

1 **Measurement report: Validation of multi-satellite remote sensing**
2 **products and potential source apportionment of BrO and IO in the**
3 **Arctic using ship-based DOAS**

4 Qijin Zhang^{1,2}, Chengzhi Xing^{2,*}, Yikai Li^{2,5}, Haochen Peng^{1,2}, Haoran Liu⁶, Chao Liu^{1,2}, Zhiguo
5 Zhang^{1,2}, Wanchao Ma¹, Tianyu Tang¹, Cheng Liu^{1,2,3,4,*}

6 ¹Department of Precision Machinery and Precision Instrumentation, University of Science and
7 Technology of China, Hefei 230026, China

8 ²Key Lab of Environmental Optics & Technology, Anhui Institute of Optics and Fine Mechanics,
9 Hefei Institutes of Physical Science, Chinese Academy of Sciences, Hefei 230031, China

10 ³Center for Excellence in Regional Atmospheric Environment, Institute of Urban Environment,
11 Chinese Academy of Sciences, Xiamen 361021, China

12 ⁴Key Laboratory of Precision Scientific Instrumentation of Anhui Higher Education Institutes,
13 University of Science and Technology of China, Hefei 230026, China

14 ⁵School of Environmental Science and Optoelectronic Technology, University of Science and
15 Technology of China, Hefei 230026, China

16 ⁶Information Materials and Intelligent Sensing Laboratory of Anhui Province, Institutes of Physical
17 Science and Information Technology, Anhui University, Hefei, 230601, China

18 Corresponding authors: xingcz@aiofm.ac.cn; chliu81@ustc.edu.cn

19

20 **Abstract:**

21 Arctic reactive halogen species (RHS) are pivotal in mediating polar air-sea interactions and
22 global biogeochemical cycling. Based on ship-borne MAX-DOAS observations from the 12th
23 Chinese National Arctic Research Expedition (July to September 2021), this study provides a
24 systematic performance assessment of TROPOMI, GEMS, and GOME-2 satellite products in the
25 Arctic ($R > 0.6$). Our findings indicate that tropospheric BrO variability is predominantly governed
26 by sea-ice contact (SIC) duration, accounting for 48.63% of the variance in a Generalized Additive
27 Model (GAM). Potential BrO source regions are identified in western Greenland, the high-latitude
28 Canadian Arctic, and the Marginal Ice Zone (MIZ). Implementing a dynamic boundary layer height
29 (BLH) constraint enhanced the correlation from 0.73 to 0.77. Meteorological conditions exert
30 significant modulation on activation efficiency. For instance, correlations reached 0.84 under
31 southwesterly flow, whereas snowfall reduced the correlation from 0.84 during snow-free periods
32 to 0.61 during snowfall events. Conversely, IO spatial variability is primarily driven by marine
33 biogenic emissions, exhibiting a positive correlation with chlorophyll-a concentrations ($R = 0.64$)
34 and clustering in phytoplankton-rich regions such as the Bering Strait. In the MIZ, the moderate

35 correlation between BrO and IO ($R = 0.5$) suggests their co-evolution at the shared ice-ocean-
36 atmosphere interface. These high-resolution datasets provide critical a priori constraints for
37 atmospheric chemistry models. Specifically, they facilitate the optimization of polar emission
38 parameterizations and reactive halogen budgets, thereby enhancing the predictive accuracy of
39 GEOS-Chem and WRF-Chem for polar atmospheric processes and improving the robustness of
40 global climate assessments.

41 **1. Introduction**

42 The unique geographic and climatic conditions of the polar regions make them sensitive
43 indicators and amplifiers for global climate change and atmospheric chemistry. They play an
44 irreplaceable role in regulating global ozone balance, aerosol cycles, and air-sea interactions
45 (Polvani et al., 2020). Nitrogen oxides (NO_x), formaldehyde (HCHO), and RHS, including X, HOX,
46 XY, OXO, XNO₂, X₂, XO, and XONO₂, where Y and X represent halogen atoms such as I and Br
47 are core components of polar atmospheric chemistry (Hara et al., 2020; Saiz-Lopez et al., 2008).
48 Halogen radicals (e.g., Br, I, Cl) drive polar ozone depletion catalytically (Hara et al., 2020; Polvani
49 et al., 2020), while RHS also modulate the HO_x and NO_x ratios (Bloss et al., 2005; Khosravi et al.,
50 2020; Ranjithkumar et al., 2023). XO radicals oxidize NO to NO₂, thus increasing the NO_x ratio; in
51 contrast, they react with HO₂ to form HOX, which subsequently undergoes photolysis (a process
52 particularly efficient for HOI) to generate OH, thereby decreasing the HO_x ratio (Saiz-Lopez et al.,
53 2007; Welsh et al., 2023). The bromine explosion process on saline surfaces covered by sea ice or
54 snow converts bromide ions (Br^-) into gaseous reactive bromine species, serving as the primary
55 source of bromine in the polar boundary layer (Hara et al., 2020; Saiz-Lopez et al., 2007). In contrast,
56 iodine oxides (IO) originate mainly from marine phytoplankton, with their concentrations tightly
57 linked to polar ecosystem dynamics (Cuevas et al., 2018). Fig. S1 illustrates the key chemical cycles
58 of iodine and bromine in the polar troposphere.

59 Currently, polar atmospheric composition observations primarily rely on satellite remote
60 sensing (Begoïn et al., 2010; Blechschmidt et al., 2016; Bougoudis et al., 2020; Dameris et al., 2021;
61 De Laat et al., 2024; Hindley et al., 2019; Mahajan et al., 2021; Roy et al., 2024; Seo et al., 2020;
62 Yang et al., 2021) and ground-based station measurements (Crutzen, 1970; Frieß et al., 2010, 2011;
63 Gong et al., 2025; Hao et al., 2025; Luo et al., 2018; Mahajan et al., 2021, 2024; Prados-Roman et
64 al., 2018), yet both suffer from notable limitations. While satellite remote sensing enables large scale
65 coverage, the unique high albedo snow and ice surfaces, extreme low temperatures, and high cloud
66 cover in polar regions limit its retrieval accuracy for trace gases, particularly low concentration BrO
67 and IO. Furthermore, the spatiotemporal resolution of satellites is insufficient to capture the rapid
68 dynamics of polar photochemical reactions (e.g., reactive bromine radicals have lifetimes as short
69 as minutes), precluding real-time tracking of short-term trace gas variations (Wagner et al., 2007).
70 Ground-based stations deliver high resolution data but are predominantly located in terrestrial or
71 island regions of Antarctica and the Arctic (Frieß et al., 2011; Luo et al., 2018; Prados-Roman et al.,

72 2018; Simpson et al., 2017; Yang et al., 2020). Since approximately 70% of polar areas consist of
73 oceans, data on NO₂, HCHO, and BrO in the marine boundary layer are scarce. This scarcity means
74 satellite retrieval results over oceanic regions lack effective validation.

75 Additionally, regional studies of reactive halogen species exhibit distinct gaps: most research
76 on BrO and IO focuses on local regions like the Antarctic Peninsula and Arctic Svalbard (Adachi et
77 al., 2022; Čížková et al., 2023; Luo et al., 2018; Mahajan et al., 2024; Park et al., 2023; Spagnesi et
78 al., 2024), with ship-based DOAS data missing for extensive oceanic areas such as the Arctic
79 Chukchi and Beaufort Seas. Extensive literature over the past few decades has established the
80 foundation for research on polar halogen activation (Brockway et al., 2024; Luo et al., 2018;
81 Peterson et al., 2017; Pratt et al., 2013; Swanson et al., 2020; Wagner et al., 2007), particularly
82 regarding the distribution and underlying mechanisms of reactive halogens during the polar spring.
83 Specifically, Pratt et al. (2013) confirmed the photochemical production of Br₂ from sunlit snowpack,
84 while Swanson et al. (2020) identified distinct environmental patterns of reactive bromine events
85 through long-term ground-based observations. However, existing datasets primarily analyze
86 springtime data and are concentrated at stationary sites such as Alert, Utqiagvik, and Ny-Ålesund.
87 Observational evidence for the summer melt season remains scarce, leaving the evolution
88 mechanisms of the halogen cycle under continuous high-radiation conditions unclear. Thus, there is
89 an urgent need for mobile, high spatiotemporal resolution on-site detection techniques to resolve
90 polar boundary layer chemical processes and accurately identify the sources and transformations of
91 halogen species. Ship-based Multi-Axis Differential Optical Absorption Spectroscopy (MAX-
92 DOAS) is well suited to address this gap: by collecting scattered sunlight from multiple directions,
93 it retrieves IO, BrO, HCHO, and other trace gases from the ultraviolet visible spectrum. Moreover,
94 it enables point-line integrated mobile observations aboard research vessels, serving as a robust tool
95 for studying atmospheric composition in polar oceanic regions (Nasse et al., 2015a, b; Wagner et
96 al., 2007).

97 In recent years, Arctic sea-ice extent has exhibited a significant declining trend, which directly
98 impacts key processes in polar atmospheric chemistry (e.g., the extent and intensity of bromine
99 explosions). Significant reductions in Arctic sea-ice extent and concentration were observed in
100 August 2021, particularly in the Beaufort Sea and Bering Strait (Fig. S2). These changes alter the
101 saline water-sea surface-atmosphere exchange interface and influence marine phytoplankton
102 distribution, which may further modulate the release and formation of reactive halogen species.

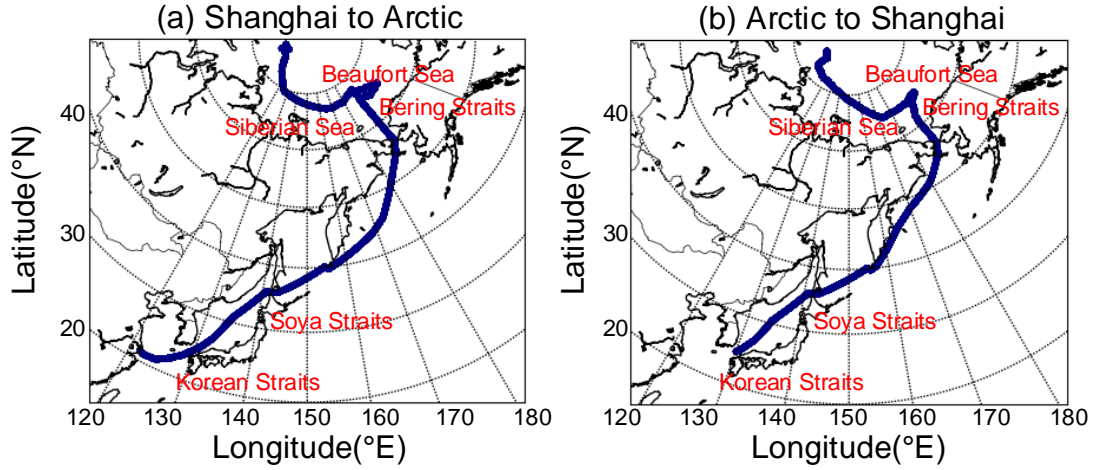
103 Leveraging the ship-based MAX-DOAS measurements aboard the Xuelong 2 during China's
104 12th Arctic Scientific Expedition (2021), this study pursued the following objectives consistent with
105 the nature of a Measurement Report: 1) Evaluate the polar applicability of NO₂, HCHO, and BrO
106 satellite products by providing a high-precision on-site benchmark for validating retrieval
107 uncertainties in polar oceanic regions. 2) The sea-ice-driven mechanism governing tropospheric
108 BrO was validated, with the quantification of sea-ice contact (SIC) duration refined by incorporating

109 boundary layer height constraints. Furthermore, Generalized Additive Models (GAMs) were
110 employed to elucidate the synergistic influences of meteorological parameters and sea-ice surface
111 characteristics on the BrO - SIC relationship. 3) Verify the biogenic driving mechanism of IO
112 concentrations by quantifying its correlation with MODIS-derived chlorophyll-a and revealing the
113 spatial differentiation between sea-ice-derived BrO and biogenic IO. By filling critical observational
114 gaps in the Arctic marine boundary layer, this report provides essential empirical constraints for
115 upgrading the parameterizations of halogen chemical cycles in atmospheric chemistry models (e.g.,
116 GEOS-Chem and WRF-Chem), thereby enhancing the accuracy of polar air-sea interaction
117 simulations and global climate assessments.

118 **2. Experiment**

119 **2.1 Experimental Setup**

120 The instrument was installed on the research vessel Xuelong 2 on July 10, 2021, and performed
121 continuous automated measurements throughout the cruise. The vessel departed Shanghai Port
122 (31.35°N, 121.69°E) on July 12, 2021, sailing via the Korea Strait, Soya Strait, Bering Strait,
123 Beaufort Sea, and Siberian Seas (see Fig. 1 for the detailed trajectory). The time of the first contact
124 with sea ice was July 24 (72.20°N, 169.18°W); subsequently, the vessel sailed toward the Arctic
125 region and began its return voyage on August 28, 2021. The instrument was fixed on the vessel's
126 side deck, mounted away from the ship's exhaust vents with an unobstructed surrounding field of
127 view (Tan et al., 2018). During ship-based mobile measurements, the observation azimuth was
128 directed toward the stern (see Fig. S3 for the vessel's top view). The ship-based MAX-DOAS system
129 comprises a motor driven observation unit, a spectrometer operating in the 300-460 nm range
130 (spectral resolution: 0.6 nm), a temperature control system, and a computer control unit. For
131 measurements, right angle prisms reflect scattered sunlight at different elevation angles; this light is
132 transmitted to the spectrometer via optical fibers for spectral acquisition, and the computer control
133 unit performs spectral analysis. The temperature control system ensured stable instrument operation
134 under the Arctic's extreme cold conditions. Ship sway caused the telescope's elevation angle relative
135 to the vessel to deviate from the actual observation direction. To mitigate this effect, the spectral
136 exposure time was set to 100 ms, which is short enough that ship movement during spectral
137 recording was negligible. Additionally, the observation elevation angle sequence was set to 10°, 20°,
138 and 90° (zenith) to reduce the impact of ship roll on the observed spectra. The system was also
139 equipped with a high precision Global Positioning System to log the vessel's real time cruise
140 coordinates and trajectory.



141

142 **Fig. 1.** Trajectories of the research vessel for the 12th Arctic Scientific Expedition: (a) Go from
 143 Shanghai to the Arctic; (b) Return from the Arctic

144 **2.2 Data Analysis**

145 **2.2.1 Data Processing and Filtering**

146 Data retrieval was conducted using the QDOAS software (BIRA-IASB; [http://uv-](http://uv-vis.aeronomie.be/software/QDOAS)
 147 [vis.aeronomie.be/software/QDOAS](http://uv-vis.aeronomie.be/software/QDOAS)) based on the DOAS principle. For ship-based spectral
 148 processing, offset corrections and dark current were first applied to the data. During retrieval, zenith
 149 spectra for each elevation angle sequence were used as reference spectra. Detailed retrieval
 150 parameters are provided in Table 1, with retrieval configurations following previous studies (Frieß
 151 et al., 2023; Hong et al., 2018; Mahajan et al., 2021; Saiz-Lopez et al., 2008). A 5th-order
 152 polynomial was used to remove broad band structures induced by Mie and Rayleigh scattering,
 153 while a nonlinear intensity offset was incorporated into the fitting process to mitigate the impact of
 154 instrument stray light.

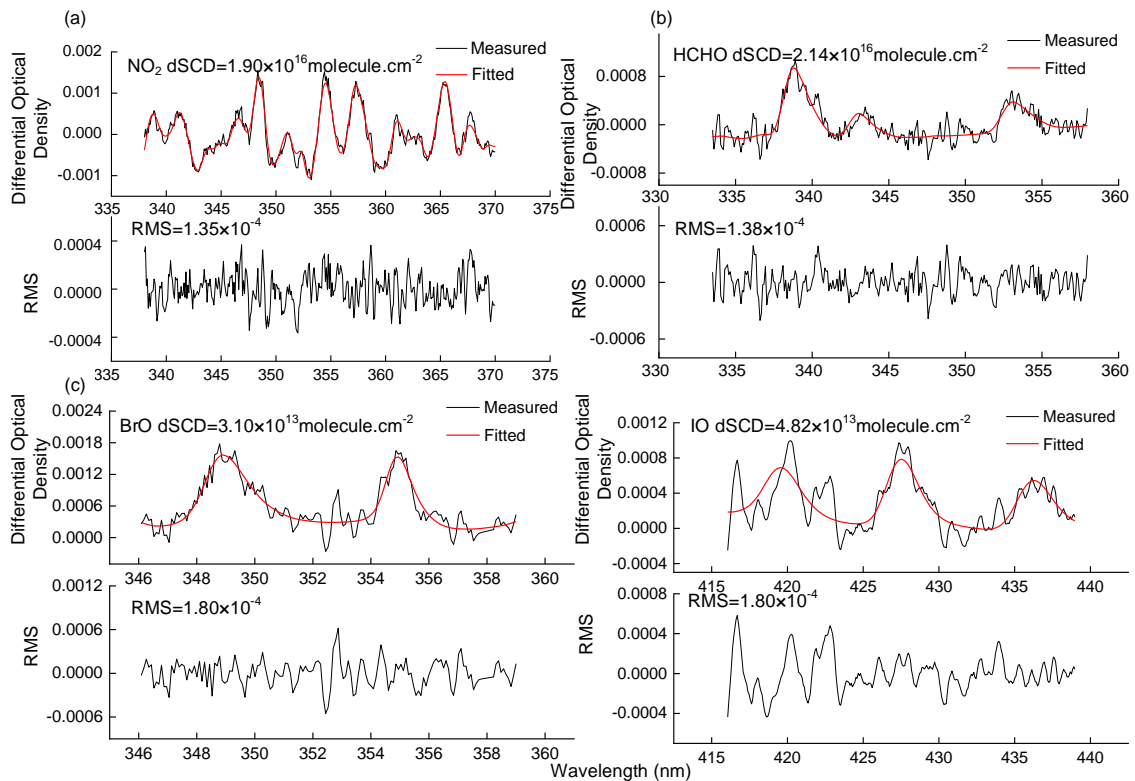
155

Table 1. Retrieval settings of IO, BrO, HCHO, and NO₂

Parameter	Reference	Fitting intervals (nm)			
		NO ₂	HCHO	BrO	IO
	Fitting wavelength	338-370	336.5-359	346-358	416-439
NO ₂ (298K)	(Vandaele et al., 1998)	√	√	√	√
NO ₂ (220K)	(Vandaele et al., 1998)	√	√	√	√
HCHO (298K)	(Meller and Moortgat, 2000)	√	√	×	√
HONO (296K)	(Stutz et al., 2000)	×	×	√	√
O ₃ (243K)	(Serdyuchenko et al., 2014)	√	×	√	√
O ₃ (223K)	(Serdyuchenko et al., 2014)	√	×	√	√
O ₄ (293K)	(Thalman and Volkamer, 2013)	√	√	√	√
BrO (223K)	(Fleischmann et al., 2004)	√	√	√	×
H ₂ O	(Rothman et al.2009)	×	×	×	√

IO	(Carlos Gómez Martín et al., 2005)	×	×	×	√
Ring	Calculated with QDOAS	√	√	√	√
Polynomial degree		5th order	5th order	5th order	3rd order
Intensity offset		Constant	Constant	Constant	Constant

156 Ship-based MAX-DOAS retrieves differential slant column densities (DSCDs) using
 157 sequential zenith reference spectra, which effectively eliminates the stratospheric background and
 158 enables the detection of tropospheric trace gases. To compensate for minor changes in spectrometer
 159 spectral calibration, spectral shift and stretching were incorporated during the fitting process. Fig. 2
 160 presents a typical spectral fitting result for a spectrum measured at 10° elevation at 1:02 UTC on
 161 August 15, 2021. Only retrieval values with a root mean square (RMS) < 3×10⁻³ and SZA < 75°
 162 were retained in this study. During mobile measurements, the ship's exhaust plume could interfere
 163 with trace gas measurements under unfavorable wind conditions. To eliminate ship exhaust
 164 interference with the spectra, spectral data measured at ship speeds below 5 km/h were filtered out,
 165 and spectra acquired under unfavorable wind conditions (0°-90° and 315°-360°) were excluded. A
 166 schematic representation of these filtering criteria is provided in Fig. S3. The filtered dataset
 167 remained adequate for robust analysis (Behrens et al., 2019).



168
 169 **Fig. 2.** An example of Ship MAX-DOAS spectral fittings for (a) NO₂, (b) HCHO, (c) BrO, and (d)
 170 IO. The spectrum was recorded at 1: 02 UTC on August 15, 2021, with an elevation of 10°.

171 **2.2.2 Uncertainties in Stratospheric-Tropospheric Separation**

172 The separation of tropospheric and stratospheric contributions using DSCDs involves several
 173 layers of uncertainty. Following established error assessment methodologies (Hendrick et al., 2007;
 174 Tack et al., 2015; Wittrock et al., 2004), the total uncertainty in our retrieved tropospheric vertical
 175 columns is attributed to two primary factors. First, spectral noise and statistical fitting uncertainties
 176 account for approximately 5% to 10% of the DSCD error under clear-sky conditions. Second,
 177 uncertainties arise from atmospheric spatial inhomogeneity and stratospheric photochemical
 178 gradients. These gradients are particularly pronounced for reactive species such as NO₂ and BrO.
 179 To mitigate this, we restricted our analysis to observations with $SZA < 75^\circ$, ensuring that the
 180 stratosphere remained in a photochemical quasi-steady state. Additionally, the implementation of a
 181 sequential zenith reference spectrum (ZRS) within short intervals (a few minutes) effectively
 182 minimizes the influence of stratospheric temporal and spatial variability. In the Arctic environment,
 183 the residual error stemming from stratospheric gradients following the sequential ZRS subtraction
 184 is estimated to be less than 10%.

185 Based on these components, the combined uncertainty for the tropospheric and stratospheric
 186 separation during this campaign ranges from 11.2% to 14.1%. We note that the relative uncertainty
 187 may increase in the pristine Arctic atmosphere when tropospheric abundances are near detection
 188 limits.

189 **2.2.3 Retrieval of Trace Gas Vertical Column Densities**

190 Because DOAS analysis yielded DSCDs in this study, conversion to vertical column densities
 191 (VCDs) required the application of differential atmospheric air mass factors, and the specific
 192 formula is given below:

$$\begin{aligned}
 DSCD_{trop}(\alpha) &= SCD_{trop}(\alpha) - SCD_{trop}(90^\circ) \\
 &= AMF_{trop}(\alpha) \times VCD_{trop} - AMF_{trop}(90^\circ) \times VCD_{trop} \\
 \Rightarrow VCD_{trop} &= \frac{DSCD_{trop}(\alpha)}{DAMF_{trop}(\alpha)}
 \end{aligned}
 \tag{1}$$

194 In the above equation, α denotes the telescope observation angle, and $DAMF_{trop}(\alpha)$ is
 195 expressed as $AMF_{trop}(\alpha) - AMF_{trop}(90^\circ)$. Owing to rapidly changing radiative conditions and
 196 heterogeneous air masses encountered during ship-based MAX-DOAS campaigns, an alternative
 197 retrieval method was developed for mobile platforms. This method, which has been successfully
 198 applied in previous mobile MAX-DOAS studies (Hong et al., 2018; Wagner et al., 2010),
 199 demonstrates superior performance over the standard approach. Therefore, this study adopts this
 200 method to retrieve tropospheric VCDs, with the specific formula provided below:

$$\begin{aligned}
 VCD_{trop} &= \frac{SCD_{meas}(\alpha) - SCD_{strat}(SZA)}{AMF_{trop}(\alpha)} \\
 &= \frac{DSCD_{meas}(\alpha) + SCD_{ref} - SCD_{strat}(SZA)}{AMF_{trop}(\alpha)}
 \end{aligned}
 \tag{2}$$

202 In the above equation, SZA denotes the Solar Zenith Angle. The difference between SCD_{ref}

203 and $\text{SCD}_{\text{strat}}$ (SZA) two unknowns) is defined as $\text{DSCD}_{\text{offset}}$. Combining Equations (1) and (2)
 204 yields the specific expression for $\text{DSCD}_{\text{offset}}$.

$$205 \quad \text{DSCD}_{\text{offset}} = \frac{\text{DSCD}_{\text{meas}}(\alpha) \times \text{AMF}_{\text{trop}}(90^\circ) - \text{DSCD}_{\text{meas}}(90^\circ) \times \text{AMF}_{\text{trop}}(\alpha)}{\text{AMF}_{\text{trop}}(\alpha) - \text{AMF}_{\text{trop}}(90^\circ)} \quad (3)$$

206 Here, $\text{DSCD}_{\text{offset}}$ is a time smooth function, fitted to the $\text{DSCD}_{\text{offset}}(t_i)$ time series using a second
 207 order polynomial, where t_i denotes the time interval between two spectra at a given observation
 208 angle. The calculated $\text{DSCD}_{\text{offset}}(t_i)$ time series is expressed as:

$$209 \quad \begin{aligned} & \text{DSCD}_{\text{offset}}(t_i) \\ & = \frac{\text{DSCD}_{\text{meas}}(\alpha, t_i) \times \text{AMF}_{\text{trop}}(90^\circ, t_i) - \text{DSCD}_{\text{meas}}(90^\circ, t_i) \times \text{AMF}_{\text{trop}}(\alpha, t_i)}{\text{AMF}_{\text{trop}}(\alpha, t_i) - \text{AMF}_{\text{trop}}(90^\circ, t_i)} \end{aligned} \quad (4)$$

210 The fitted polynomial approximates $\text{DSCD}_{\text{offset}}(t_i)$; substituting it into Equation (2) gives the
 211 tropospheric VCD time series. Details of this method are provided in Wagner et al. (2010). Radiative
 212 calculations in this study were conducted with the atmospheric radiative transfer model SCIATRAN
 213 2.2 (Rozanov et al., 2005).

214 **2.3 Performance of the MAX-DOAS Retrieval**

215 **2.3.1 Uncertainty Analysis**

216 Following established methodologies (Hendrick et al., 2007; Song et al., 2023; Tack et al.,
 217 2015; Wagner et al., 2007; Wittrock et al., 2004), the uncertainty in MAX-DOAS retrievals is
 218 categorized into four primary sources. First, smoothing and noise errors originate from statistical
 219 uncertainties in the DOAS fitting. Under clear-sky conditions, the fitting errors for NO_2 , HCHO,
 220 BrO, and IO remain within 5% to 10%. Second, reference spectrum uncertainty arises because
 221 tropospheric DSCDs are determined by subtracting a sequential ZRS from off-axis measurements.
 222 While this approach assumes stratospheric absorption cancels out, uncertainties in the residual trace
 223 gas abundances within the ZRS (stemming from stratospheric background or tropospheric pollution)
 224 can introduce systematic biases of approximately 10% to 15%. Third, algorithmic errors primarily
 225 stem from uncertainties in aerosol vertical distribution, multiple scattering simulations, and profile
 226 assumptions within the radiative transfer model. For the Arctic sea-ice environment, sensitivity tests
 227 demonstrate that surface albedo has a negligible impact on boundary layer observations at low
 228 elevation angles, with the total AMF uncertainty estimated at 10% to 20%. Fourth, residual errors
 229 from stratospheric gradients and atmospheric inhomogeneity are considered. By employing the
 230 sequential ZRS method and filtering for $\text{SZA} < 75^\circ$, errors from steep stratospheric photochemical
 231 gradients are effectively suppressed to within 10%.

232 Consequently, the total uncertainty of the retrieved VCDs during this ship-based campaign is
 233 estimated to be approximately 18.1% to 28.7%. Furthermore, due to the pristine background of the
 234 Arctic region, the relative proportion of this uncertainty may increase when tropospheric
 235 concentrations are extremely low. Detailed information is provided in the supplement (Table S1).

236 2.3.2 Detection Limits

237 To evaluate the sensitivity of MAX-DOAS in the Arctic environment, different methods were
238 adopted to calculate detection limits based on the atmospheric distribution and signal-to-noise ratio
239 characteristics of various trace gases. First, for NO₂, HCHO, and IO, we used the standard method
240 in DOAS applications to determine the detection limit (Chance and Spurr, 1997; Stutz and Platt,
241 1996; Wagner et al., 2007). The detection limit of the DSCD (LOD_{dSCD}) is defined as twice the
242 statistical fitting error from the DOAS retrieval ($2\sigma_{fit}$). Second, for BrO, since tropospheric BrO
243 concentrations in the Arctic are relatively low and influenced by the stratospheric BrO background,
244 the conventional $2\sigma_{fit}$ noise method often over estimates the tropospheric detection limit because
245 of the high weighting of stratospheric absorption. Therefore, we adopted the equivalent RMS noise
246 factor method, which calculates the minimum identifiable slant column density at a given signal-to-
247 noise ratio by analyzing the RMS noise of the residual spectrum (Coburn et al., 2011). During the
248 observation period, the estimated detection limits for NO₂, HCHO, BrO, and IO were 2.0×10^{15}
249 molec.cm⁻², 5.0×10^{15} molec.cm⁻², 3.0×10^{13} molec.cm⁻², 1.3×10^{13} molec.cm⁻², respectively.

250 2.4 Satellite Observations

251 This study compares ship-based MAX-DOAS measurements with tropospheric VCD products
252 from multiple satellite instruments, including the Tropospheric Monitoring Instrument (TROPOMI),
253 Geostationary Environmental Monitoring Spectrometer (GEMS), and Global Ozone Monitoring
254 Experiment-2 (GOME-2).

255 TROPOMI is onboard the Sentinel-5P (S-5P) satellite, operating in a near Earth sun
256 synchronous orbit with an equator crossing time of 13:30 local time. It features 4 independent
257 spectrometers covering the mid-ultraviolet (UV), long wave UV-visible (UV-VIS), short-wave
258 infrared (SWIR), and near infrared (NIR) bands, with a total wavelength range of 270-2385 nm
259 (non-overlapping and discontinuous). Among comparable atmospheric remote sensing instruments,
260 TROPOMI has the best spatial resolution ($5.5 \text{ km} \times 3.5 \text{ km}$), enabling precise capture of spatial
261 distributions of trace gases in small scale regions, making it a key data source for high resolution
262 atmospheric composition monitoring in polar oceans.

263 GEMS is a hyperspectral UV-VIS imaging spectrometer onboard the Cheollima-2 satellite,
264 operating in a geostationary orbit and focusing on atmospheric trace gas observations over the Asia
265 Pacific. With a spatial resolution of $3.5 \text{ km} \times 8 \text{ km}$, it effectively monitors trace gases like HCHO
266 and NO₂; additionally, its high temporal resolution (one regional scan per hour) captures short term
267 dynamic changes in atmospheric composition, offering temporal insights into rapid polar
268 photochemical processes.

269 The GOME-2 series (GOME-2A, GOME-2B) are onboard the sun-synchronous MetOp
270 satellite, with an equator crossing time of 09:30 local time. They measure by receiving sunlight
271 reflected from the Earth's atmosphere or surface, covering 240-790 nm. Despite a relatively low
272 spatial resolution ($40 \text{ km} \times 40 \text{ km}$), they retrieve auxiliary parameters such as cloud top pressure

273 (CTP) and effective cloud fraction via the Fast Retrieval Scheme for Clouds from the Oxygen A
 274 band (FRESCO+), supporting quality control for atmospheric composition retrieval in cloudy
 275 regions. In this study, tropospheric BrO VCD analysis uses GOME-2B products to investigate large
 276 scale polar BrO distribution.

277 Scanning Imaging Absorption Spectrometer for Atmospheric Chartography was one of the core
 278 payloads aboard the European Space Agency (ESA)'s Envisat satellite, with its operation directly
 279 tied to the satellite platform. On 8 April 2012, Envisat suffered an unexpected loss of contact;
 280 subsequently, on 9 May 2012, ESA officially declared the mission terminated, and SCIAMACHY
 281 ceased operations alongside the platform. Owing to this constraint, satellite validation of
 282 atmospheric IO observations was not performed in this study.

283 **2.5 Potential Source Contribution Function**

284 The PSCF is a Lagrangian receptor-oriented model employed to pinpoint potential emission
 285 source areas. For a specific grid cell (i, j), the PSCF value is defined as the ratio of the number of
 286 "polluted" trajectory endpoints ($m_{i,j}$), associated with concentrations exceeding a predefined
 287 threshold) to the total number of endpoints ($n_{i,j}$) residing in that cell.

$$288 \quad \text{PSCF}_{i,j} = \frac{m_{i,j}}{n_{i,j}} \quad (5)$$

289 To reduce uncertainty caused by small grid counts, this study refers to Pernov et al., (2021), Polissar
 290 et al., (2001), Yin et al., (2018) by introducing a weight function to obtain the weighted PSCF
 291 (WPSCF). The formula is as follows:

$$292 \quad \text{WPSCF}_{i,j} = W(n_{i,j}) \times \text{PSCF}_{i,j}$$

$$W(n_{i,j}) = \begin{cases} 1.00 & n_{i,j} > n_{avg} \\ 0.70 & n_{avg} / 3 < n_{i,j} \leq n_{avg} \\ 0.42 & n_{avg} / 5 < n_{i,j} \leq n_{avg} / 3 \\ 0.17 & n_{i,j} \leq n_{avg} / 5 \end{cases} \quad (6)$$

293 Where n_{avg} represents the average number of endpoints across all grid cells.

294 **2.6 Auxiliary Data**

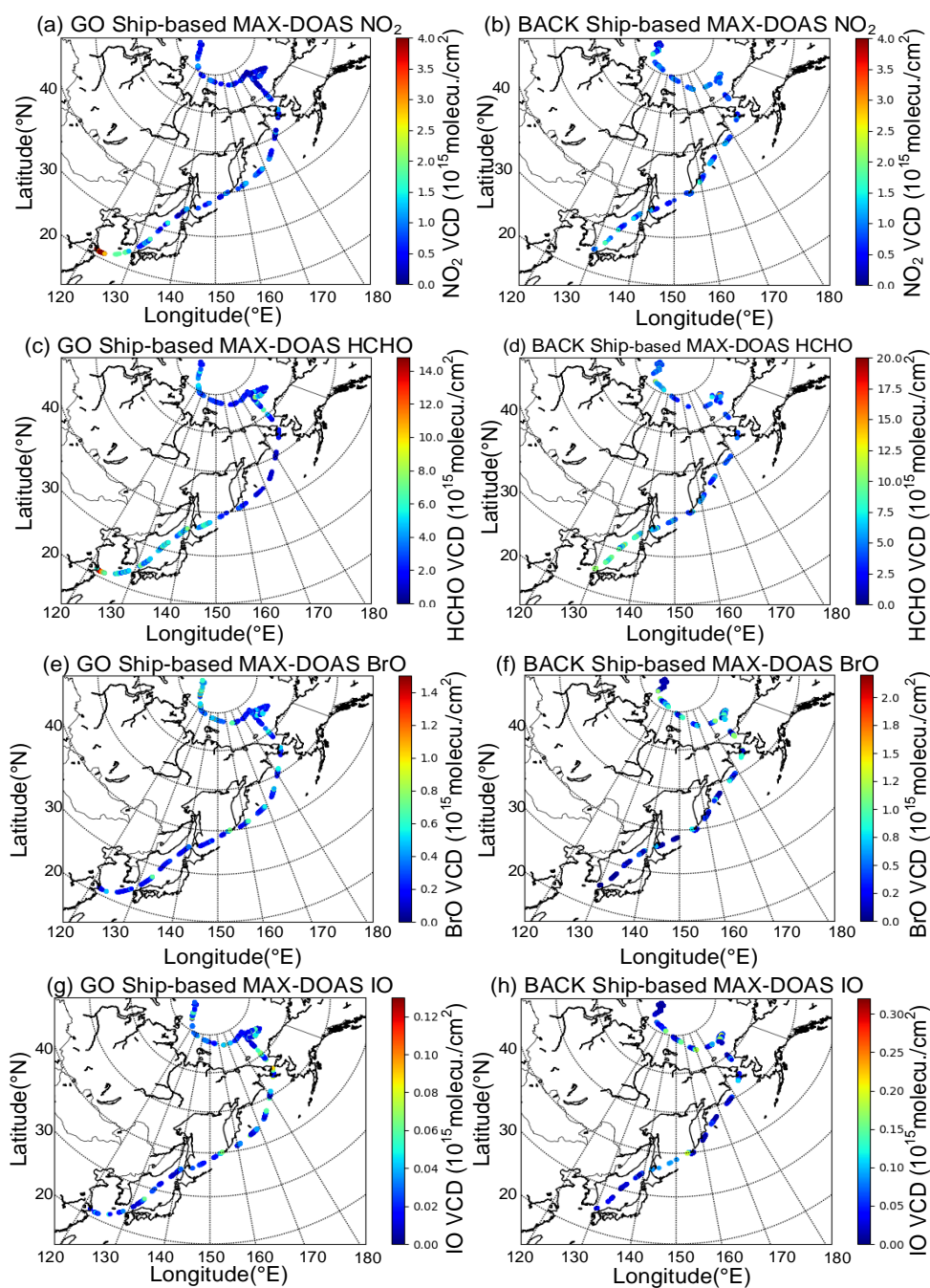
295 To estimate BrO distribution, this study obtained northern hemisphere BrO data from GOME-
 296 2 products via http://www.iup.uni-bremen.de/does/scia_data_browser.html. Sea ice concentration
 297 and age data were sourced from the National Snow and Ice Data Center. (<https://nsidc.org/home>).
 298 Chlorophyll-a concentrations were derived from Moderate Resolution Imaging Spectroradiometer
 299 (<https://aqua.nasa.gov/modis>). Backward trajectory analysis was conducted using the Hybrid Single
 300 Particle Lagrangian Integrated Trajectory model via the NASA ARL READY website to identify air
 301 mass sources. Finally, boundary layer height, wind direction, snow density, and snowfall data were
 302 obtained from the European Centre for Medium-Range Weather Forecasts (ECMWF).

303 3. Results

304 3.1 Spatial Distributions of NO₂, HCHO, BrO, and IO

305 Fig. 3 presents the spatial distributions of VCDs of four trace gases during the cruise (round
306 trip from Shanghai to the Arctic). Notably, partial data gaps exist in the cruise dataset, attributed to
307 four main interfering factors: insufficient light during nighttime navigation, spectral detection
308 interference from severe weather (e.g., thunderstorms), temporary instrument or power system
309 malfunctions, and near field data contamination by the ship's own emission plumes.

310 The high value regions of different trace gases exhibit distinct regional variations: NO₂ and
311 HCHO VCD maxima are concentrated in low latitude areas with intensive anthropogenic activities,
312 with the highest concentrations observed in the Shanghai Port region. Additionally, relatively high
313 NO₂ and HCHO concentrations are found in ports near the Korea Strait, a key shipping lane
314 connecting the Pacific Ocean and the Sea of Japan, frequented by international merchant vessels.
315 The elevated pollutant levels in these regions are likely directly linked to ship emissions from port
316 operations and shipping lanes, a mechanism supported by numerous previous studies (Hwang and
317 Kang, 2023; Wang et al., 2018). In contrast, high VCDs of the reactive halogen species IO and BrO
318 are concentrated in the Arctic Ocean. The maximum BrO VCD is observed near the Arctic Beaufort
319 Sea, while the maximum IO VCD occurs near the Arctic Bering Strait.



320

321

Fig. 3. Spatial distributions of trace gases (NO_2 , HCHO, BrO, and IO) VCDs.

322

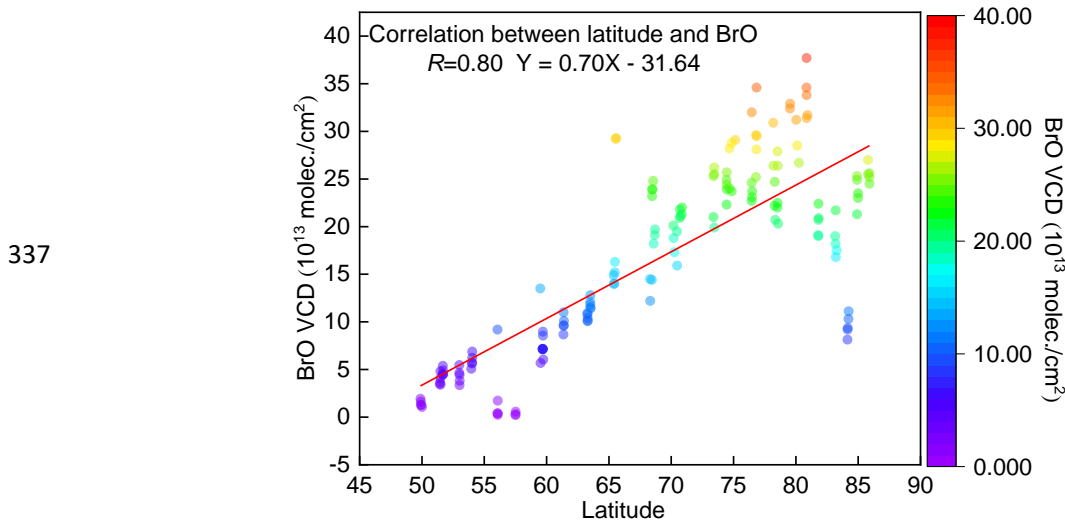
Panels (a), (c), (e), (g) present NO_2 , HCHO, BrO, and IO distributions along the go route from Shanghai to the Arctic, while panels (b), (d), (f), (h) show their distributions along the return route from the Arctic to Shanghai.

325

Fig. 3 shows that BrO concentrations generally increase with latitude. Previous studies (Simpson et al., 2007; Zhao et al., 2016) have identified high latitude Northern Hemisphere regions as cores of abnormally elevated tropospheric BrO, with these high values typically linked to key physicochemical mechanisms: sea ice photochemical processes (e.g., bromine explosion) and low temperature catalysis. Thus, this study focuses on data at and north of 50°N . Data were analyzed at 1° latitude intervals, selecting the top 5 BrO concentrations and their corresponding latitude

330

331 information per interval. As shown in Fig. 4, BrO concentrations exhibit a positive correlation with
 332 latitude, with a correlation coefficient of 0.80. In contrast, IO spatial distribution shows no distinct
 333 latitudinal gradient, suggesting its concentrations are more strongly associated with the spatial
 334 heterogeneity of marine biological activities (e.g., phytoplankton emissions). The relationship
 335 between IO and chlorophyll-a concentrations will be analyzed in depth in subsequent sections,
 336 incorporating synchronously observed marine ecological data (see Section 3.3.1 for details).



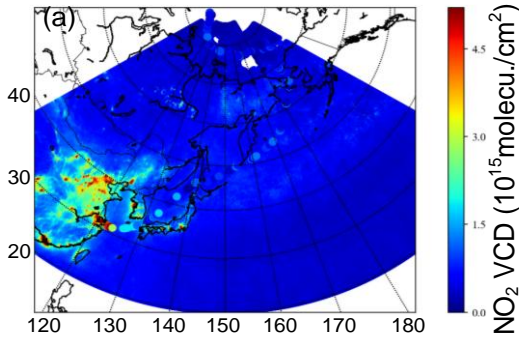
338 **Fig. 4.** BrO concentration variation observed by ship-based MAX-DOAS with latitude

339 3.2 Satellite Comparison

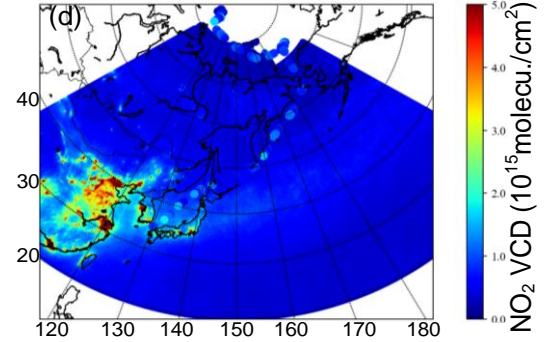
340 Ship-based MAX-DOAS measured NO₂, HCHO, and BrO VCDs were compared with
 341 atmospheric products from GEMS, TROPOMI, and GOME-2 satellites to validate the applicability
 342 of satellite data in the Arctic and adjacent seas. Results are presented in Fig. 5 (NO₂), Fig. 6 (HCHO),
 343 and Fig. 7 (BrO).

344 To ensure data reliability, satellite products with high cloud contamination (effective cloud
 345 fraction > 0.4) and poor retrieval quality (relative error > 100%) were excluded. This filtering is
 346 necessary because cloud particles significantly interfere with ultraviolet-visible radiation
 347 transmission, altering the optical path length and leading to biases in trace gas retrieval. Qualified
 348 satellite data were temporally averaged (matching the temporal resolution of ship-based
 349 observations) and interpolated to 0.1°×0.1° gridded data using a parabolic spline interpolation
 350 algorithm (Chan et al., 2015, 2018; Kuhlmann et al., 2014). This gridding process not only preserves
 351 the true spatial distribution of trace gases but also retains details of pollution hotspots (e.g., ports,
 352 shipping lanes), avoiding comparison biases from spatial scale mismatch (Hong et al., 2018). Since
 353 GEMS is focused on the Asia Pacific region and its effective detection boundary does not cover
 354 high latitude Arctic areas, it was only used for comparison within 110°E-130°E, 20°N-45°N to
 355 ensure spatial coverage consistency with ship-based observations.

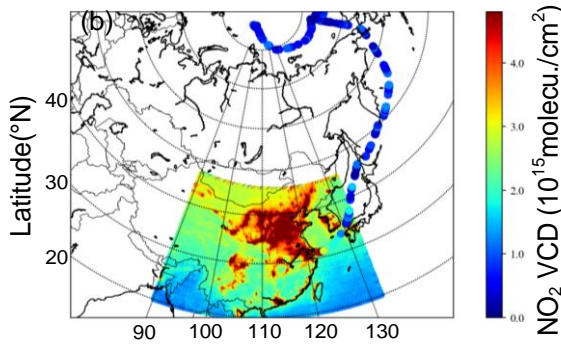
TROPOM and MAX-DOAS NO₂ VCD



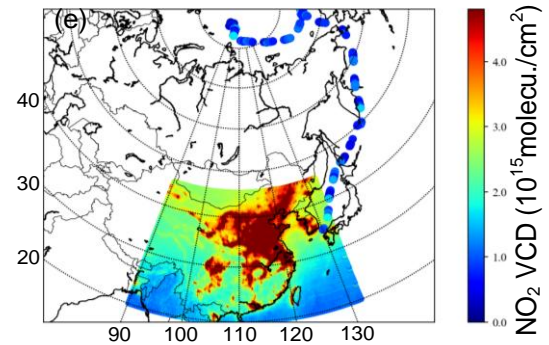
TROPOMI and MAX-DOAS NO₂ VCD



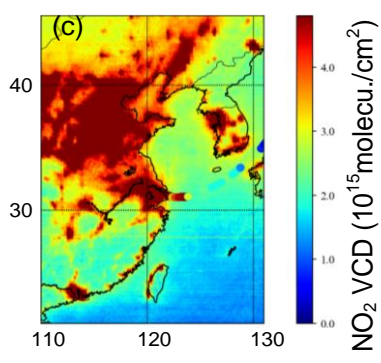
GEMS and MAX-DOAS NO₂ VCD



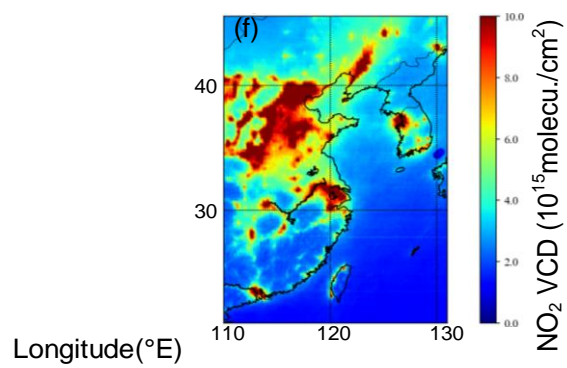
GEMS and MAX-DOAS NO₂ VCD



GEMS and MAX-DOAS NO₂ VCD



GEMS and MAX-DOAS NO₂ VCD



356

357
358

Fig. 5. Comparison of ship-based MAX-DOAS measured NO₂ VCDs with satellite observations: (a-c) Shanghai to Arctic and (d-f) Arctic to Shanghai.

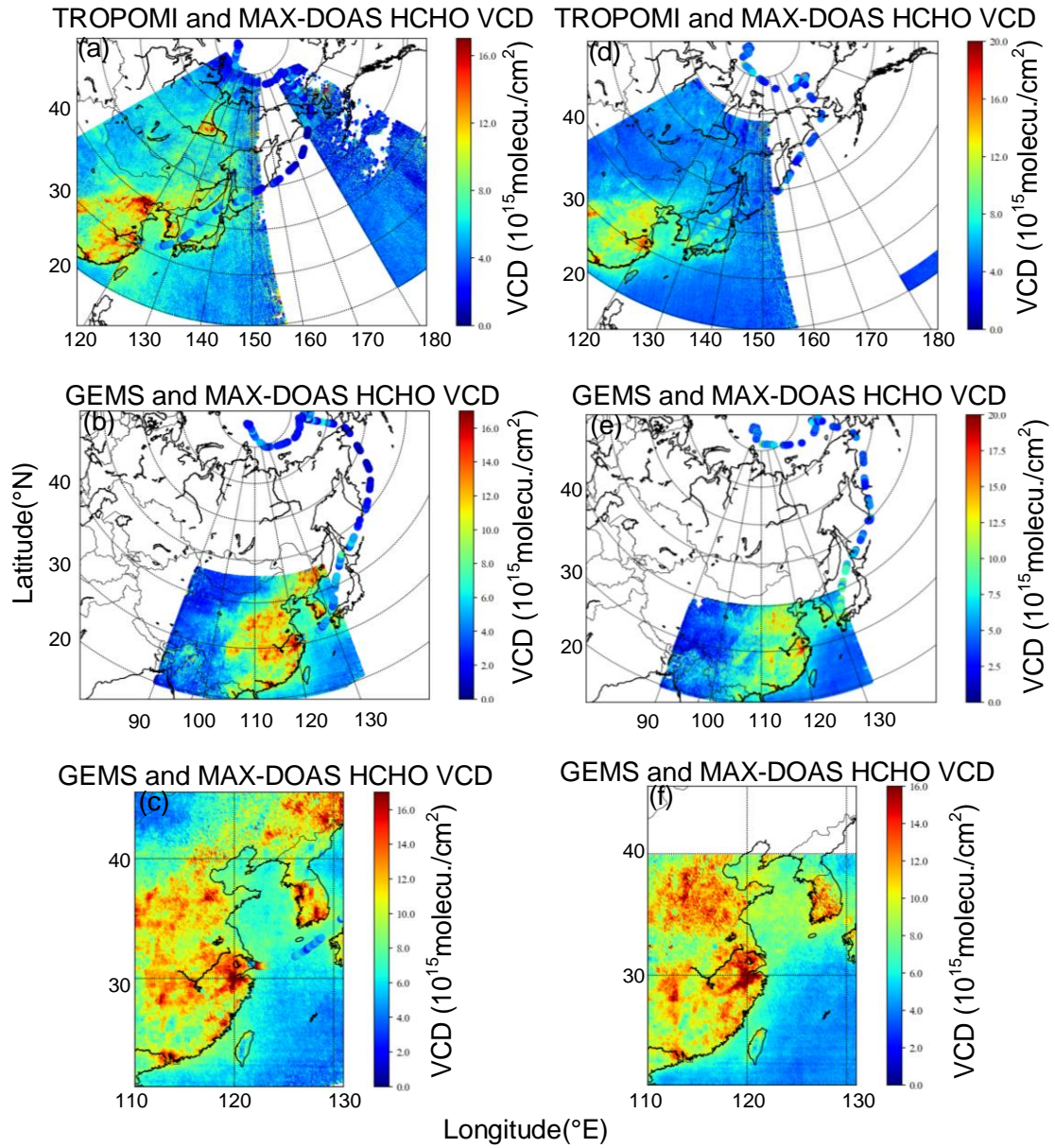


Fig. 6. Comparison of ship-based MAX-DOAS measured HCHO VCDs with satellite observations: (a-c) Shanghai to Arctic and (d-f) Arctic to Shanghai.

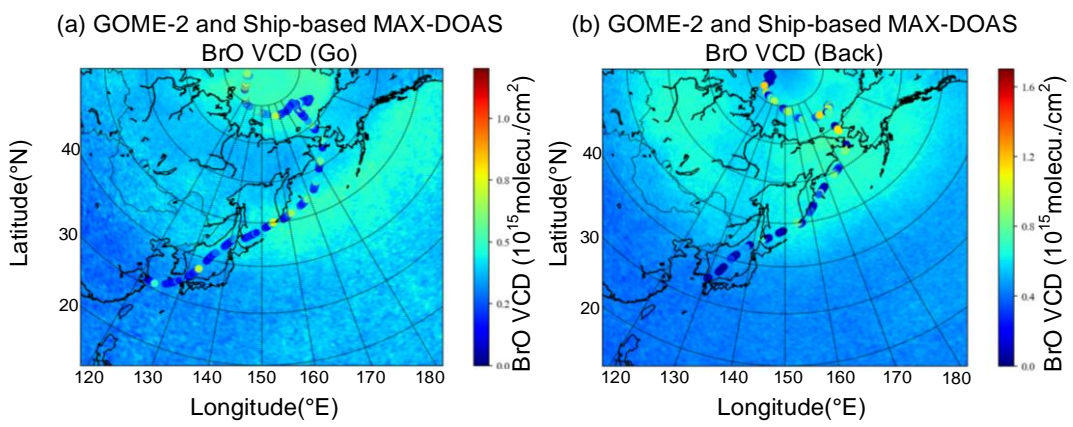
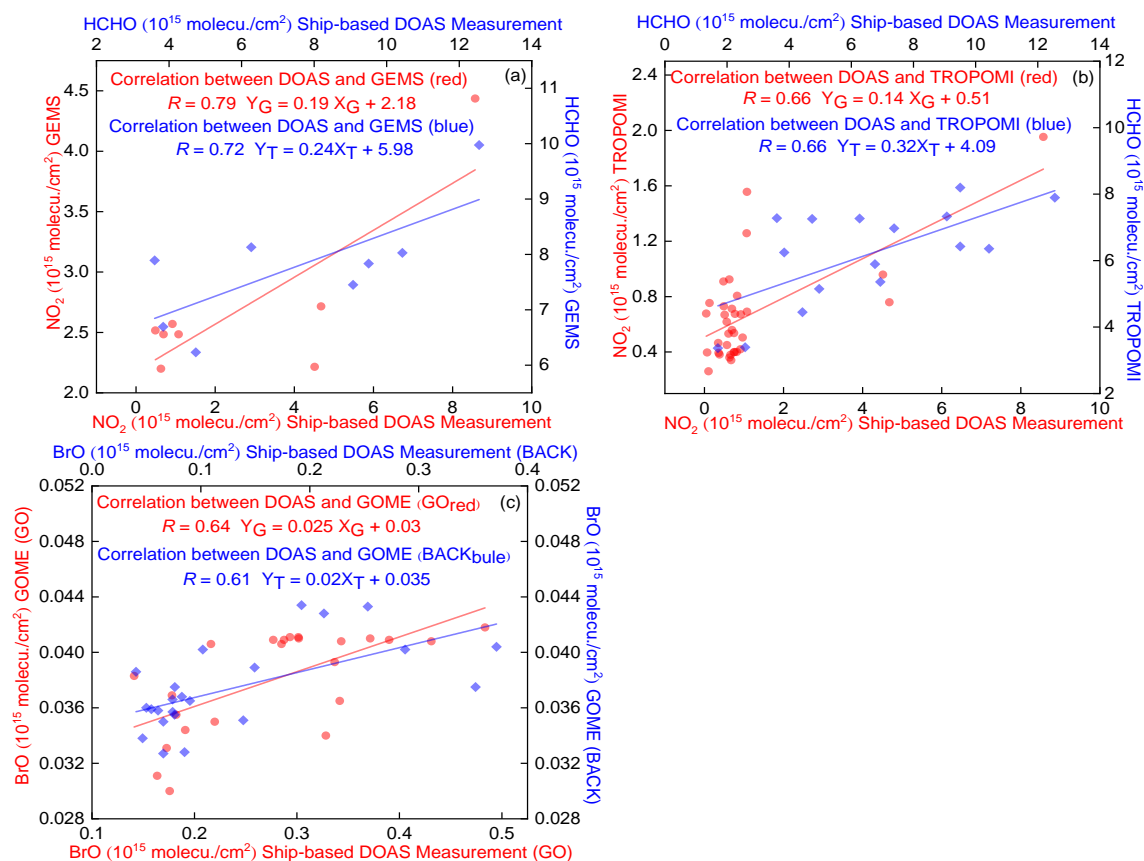


Fig. 7. Comparison of ship-based MAX-DOAS measured BrO VCDs with GOME-2 observations: (a) Shanghai to Arctic and (b) Arctic to Shanghai.

366 Direct comparisons in Figs. 5-7 reveal good overall consistency between ship-based MAX-
 367 DOAS and satellite observations (TROPOMI, GEMS, GOME-2). Notably, in mid-to-low latitude
 368 marine regions (e.g., Shanghai Port, Korea Strait), the spatial localization of HCHO and NO₂ high
 369 value areas is consistent. In Arctic regions (e.g., Beaufort Sea, Bering Strait), BrO concentration
 370 trends also exhibit clear coherence. To further quantify this consistency, satellite data were gridded
 371 and averaged over daily mobile measurement areas. Correlation analysis was performed between
 372 daily mean satellite values and daily mean mobile MAX-DOAS values throughout the cruise, with
 373 results shown in Fig. 8 (a)-(c).



374
 375 **Fig. 8.** Correlation analysis between daily measurements and satellite observations during the
 376 ship-based campaign. Panels (a) GEMS, (b) TROPOMI, (c) GOME-2.

377 Ship-based MAX-DOAS measured NO₂ and HCHO VCDs exhibit correlation coefficients of
 378 0.79 and 0.72 with GEMS satellite observations, respectively, and 0.66 for both species with
 379 TROPOMI observations. For BrO VCDs from round trip ship-based measurements, correlations
 380 with GOME-2 are 0.64 (go) and 0.61 (back). Notably, the GEMS correlation analysis uses a
 381 relatively small sample size (constrained by its observation coverage). To rule out the confounding
 382 effect of high correlation due to small sample size, TROPOMI data of the same sample size as
 383 GEMS were selected within 110°E-130°E, 20°N-45°N for recalculation (see Fig. S4). The
 384 correlation coefficient between ship-based NO₂ VCDs and TROPOMI rose to 0.73, whereas that for
 385 HCHO VCDs dropped to 0.20. This result further verifies that the strong correlation between GEMS

386 and ship-based observations does not stem from data volume deviation, but is most likely closely
387 linked to GEMS' higher temporal resolution (1 observation per hour). In contrast to TROPOMI's
388 daily observational frequency, GEMS more accurately matches the temporal dynamics of ship-
389 based MAX-DOAS measurements, mitigating concentration biases induced by time period
390 discrepancies.

391 Discrepancies between ship-based MAX-DOAS and satellite observations arise primarily from
392 three factors: 1). Satellites have substantially lower spatial resolution than ship-based MAX-DOAS
393 point scale measurements and are less sensitive to local trace gas sources (e.g., transient ship
394 emissions). In contrast, ship-based MAX-DOAS exhibits higher sensitivity to the lower atmosphere,
395 enabling precise capture of short-term emission signals from near sea surface pollutants (Wu et al.,
396 2018). This leads to slightly higher ship-based observations compared to satellite retrievals in trace
397 gas intensive regions (e.g., ports, shipping lanes). 2). Satellite retrievals are vulnerable to aerosols
398 and clouds in the Arctic and adjacent seas. Even with cloud fraction screening, cloud particles can
399 modify radiative transfer paths, resulting in underestimated trace gas absorption signals. ship-based
400 MAX-DOAS, however, partially mitigates aerosol scattering interference through multi-azimuth
401 observations, delivering more stable measurements. 3). VCDs from both platforms require
402 conversion using the AMF. AMF calculations integrate multiple variables: trace gas profiles, aerosol
403 profiles, and surface albedo. Variations in calculation assumptions thus induce VCD discrepancies.

404 **3.3 Sources of Reactive Halogen Species in the Arctic**

405 BrO and IO are core trace gases in polar atmospheric chemistry, but their emission pathways
406 and driving mechanisms show significant differences. BrO concentrations are typically influenced
407 by the coupling of physicochemical and meteorological factors, specifically the "bromine explosion
408 cycle," which involves complex heterogeneous reactions on various saline interfaces. In contrast,
409 IO in the Arctic boundary layer is mainly related to direct emissions from marine biogenic sources.
410 Therefore, this section adopts a multi-factor synergistic analysis to resolve the drivers of BrO. The
411 analysis for IO focuses on its biogenic driving attributes, emphasizing the influence of biological
412 activity, represented by chlorophyll-a, on boundary layer IO concentrations.

413 **3.3.1 Drivers and Modulating Factors of Arctic BrO**

414 To clarify the primary sources of BrO and their coupling with sea ice, this study integrated
415 satellite remote sensing data and NSIDC sea ice concentration to analyze the spatiotemporal
416 distribution of Arctic sea-ice from July to September 2021 (see Fig. S5). The results showed that
417 sea-ice was in the summer ablation phase in August: dense ice was concentrated in the central Arctic
418 Ocean and its periphery, with significant retreat of the sea ice edge zone. This spatiotemporal sea
419 ice pattern provides a basis for subsequent analyses of air mass sea ice contact duration and the
420 characteristics of the sea ice edge zone in BrO source regions. Subsequently, backward trajectory
421 analysis was performed using the HYSPLIT model to focus on the regulatory effects of air mass
422 transport paths and sea ice contact duration on reactive halogen concentrations, and to quantify the

423 impact of transport processes on source contributions. Observational data from the Xuelong research
424 vessel in the high latitude dense Arctic ice zone (August 6-30, 2021) were used, with the frequently
425 monitored representative site (86.40°N, 86.0°E) as the target location. Backward trajectories were
426 calculated every 6 hours (cutoff time: 19:00 UTC on August 30), and air mass movements were
427 simulated at three altitudes (0 m, 500 m, 1000 m) to characterize transport properties at different
428 boundary layer heights. Backward trajectory results during the ship-based MAX-DOAS campaign
429 are presented in Supplementary Fig. S6. Sea ice contact duration $T(t, h)$ is defined as the cumulative
430 time that an air mass arriving at the target location at time t and height h remains above sea ice and
431 below the threshold height z_0 . Following previous studies (Frieß et al., 2004), z_0 was set to 200 m
432 within the boundary layer's near surface mixing layer, where air undergoes sufficient exchange with
433 the sea ice surface. This facilitates BrO formation via absorption of reactive bromine or sea salt
434 aerosols (Choi et al., 2018; Jozef et al., 2024; McPhee, 2017).

435 Fig. S7 was plotted backward trajectories from the Xuelong 2 research cruise on NSIDC sea
436 ice concentration data (August 2021), with different colored curves representing air mass
437 trajectories at 0 m, 500 m, and 1000 m altitudes. Sea ice contact durations of the polluted air masses
438 were calculated using the predefined threshold height, yielding values of 30 h, 42 h, 25 h, and 18 h
439 for the dates shown in the figure. With this methodological framework established, GOME-2
440 satellite retrievals were used to derive the average BrO VCD distribution in the Arctic and adjacent
441 seas (July-September 2021; Fig. 9a). BrO concentrations exhibit a zonal gradient centered on the
442 polar region: high values are concentrated in the sea ice edge zone north of 50°N and the central
443 Arctic Ocean, while concentrations are significantly lower in mid-to-low latitudes south of 50°N.
444 This distribution aligns with the classic mechanism: brine layers on sea ice surfaces or beneath snow
445 cover provide critical reaction interfaces for the photochemical activation of halides (e.g., NaCl),
446 facilitating the multi-step conversion of bromide ions (Br^-) to gaseous BrO (Begoin et al., 2010;
447 Saiz-Lopez et al., 2008). To validate the link between source regions and latitude, the latitudinal
448 variation of BrO concentrations (July-September) was plotted (see Fig. S8). BrO concentrations
449 generally increase with latitude but slightly decrease in the near polar central region (above 85°N).
450 This phenomenon is consistent with the conclusion of Begoin et al. (2010) that Arctic BrO high
451 values are concentrated in the sea ice edge zone. This is presumably due to lower halide activation
452 efficiency in the fully ice-covered central Arctic compared to the sea ice edge zone, coupled with
453 enhanced photochemical consumption of BrO, resulting in lower concentrations (Chen et al., 2023).

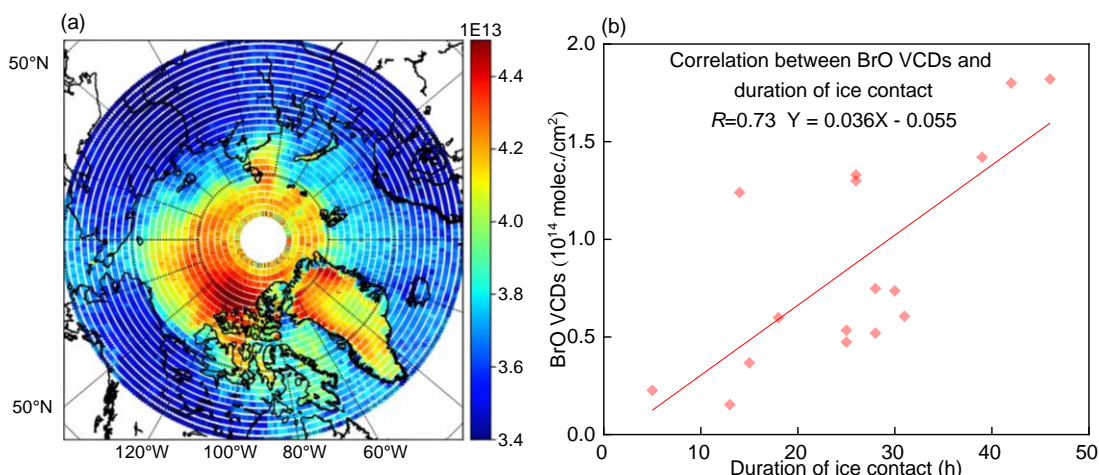


Fig. 9. Source region characteristics of Arctic BrO. (a) GOME-2 derived spatial distribution of BrO VCDs. (b) Correlation between air mass sea ice contact duration and ship-based BrO VCDs

To further validate source region characteristics, this study integrated satellite observed BrO spatial distributions with ship-based MAX-DOAS observations. Maximum daily BrO VCDs from ship-based measurements were paired with their corresponding air mass sea ice contact durations, and correlation analysis was performed (Fig. 9b). The two variables exhibit a positive correlation ($R=0.73$), consistent with the findings of Wagner et al. (2007). This indicates that the longer air masses reside over sea ice, the higher the likelihood of absorbing halides from sea ice and participating in bromine explosion events ultimately increasing BrO concentrations at the observation site (Wagner et al., 2007). This finding also explains the satellite observed pattern: BrO maxima are concentrated in the sea ice edge zone rather than the fully ice-covered central Arctic. This is attributed to intense dynamic changes in the sea ice edge zone, which enhance halide activation efficiency, and air mass transport paths in these regions are more likely to satisfy the condition of prolonged sea ice contact (Cao et al., 2024).

To elucidate the synergistic impacts of environmental parameters and quantify their respective contributions to bromine activation, we employed a Generalized Additive Model (GAM) to investigate BrO variability (see Supplement Fig. S9). The model achieved an overall correlation of $R = 0.80$. Our quantitative assessment identifies sea-ice contact time as the primary driver of BrO enhancements, accounting for an independent contribution of 48.63%. This finding statistically verifies that surface contact is the fundamental requirement for bromine activation and subsequent accumulation. Snowfall contributes 8.81% to the variance, where its negative correlation reflects the physical masking of saline source regions (e.g., frost flowers or salty snowpacks) by fresh snow, thereby inhibiting heterogeneous chemical reactions. While the direct contributions from wind direction (3.77%) and boundary layer height (3.42%) are modest, comparative sub-group analysis (e.g., $R = 0.87$ for snow-free periods versus $R = 0.61$ during snowfall) indicates that meteorological forcing primarily governs the intensity and efficiency of "bromine explosions" by modulating boundary layer stability and air mass trajectories (Bognar et al., 2020). The remaining unexplained

483 variance (35.37%) is likely associated with environmental drivers not captured in the current model.
484 Comprehensive details concerning how environmental parameters modulate the relationship
485 between BrO abundances and sea-ice contact duration are available in the Supplement Fig. S10 -
486 Fig. S17.

487 Using backward trajectory data, this study performed PSCF analysis to identify BrO's potential
488 source regions and quantify their contributions to BrO concentrations at the observation site (Fig.
489 10). To pinpoint core potential source regions, high BrO concentrations (threshold: 6.0×10^{13}
490 molec./cm²) from ship-based MAX-DOAS observations were used as the benchmark. PSCF results
491 indicate that high probability potential BrO sources are concentrated in western Greenland, the seas
492 north of North America, and the Arctic sea-ice edge zone. Sea ice dynamic processes in these regions,
493 including halide release from sea ice melting and sea salt aerosol formation and transport enhance
494 bromine activation efficiency, making them the primary contributors to BrO at the observation site
495 (Cao et al., 2024; Jozef et al., 2024) This aligns with the satellite-observed source region
496 characteristics in Section 3.3.1, further confirming that sea ice is BrO's core source.

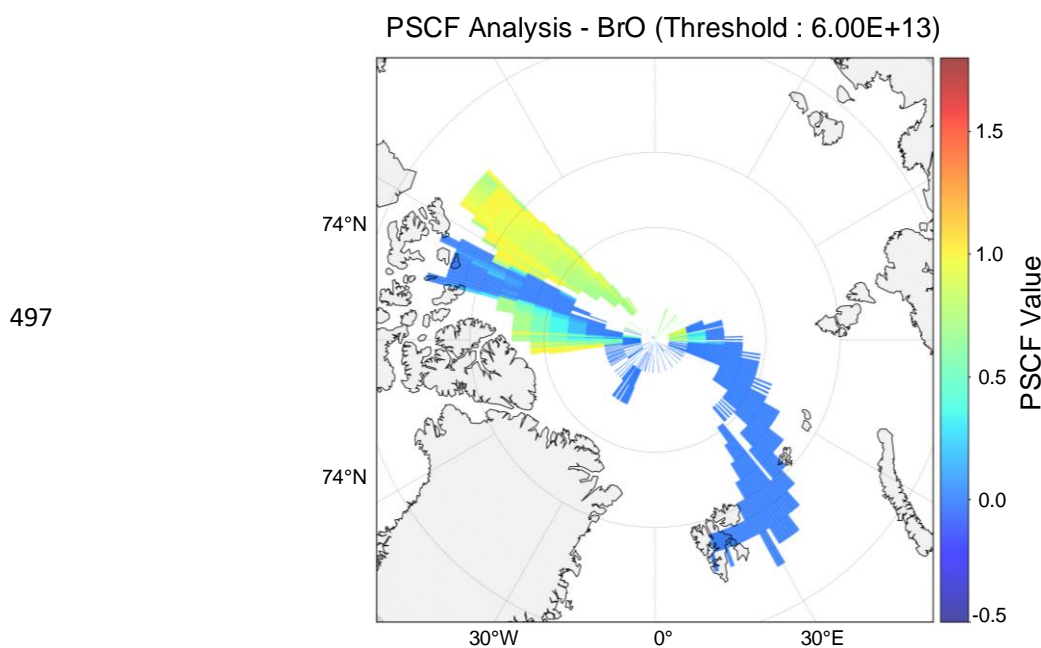


Fig. 10. PSCF analysis for BrO in the Arctic

500 3.3.2 Biogenic Sources of IO: Coupling with Chlorophyll-a Concentration

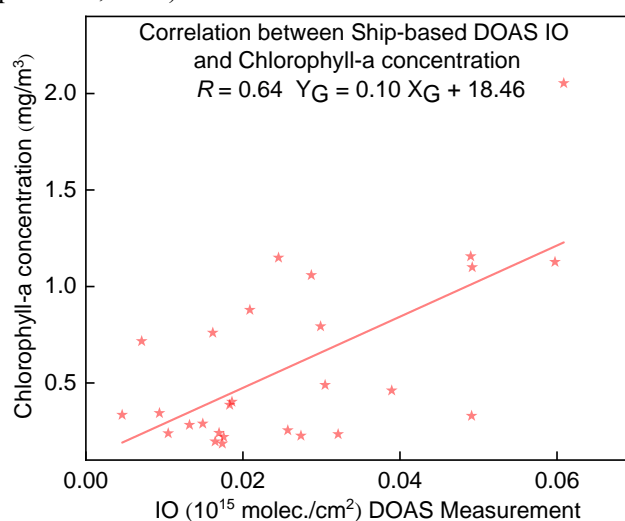
501 To address IO's sources, this study focused on its link to marine biological processes. Using
502 chlorophyll-a, which is a key indicator of phytoplankton biomass, as a proxy, we integrated MODIS
503 satellite data, ship-based observations, and backward trajectory data to assess IO's biogenic source
504 contributions from two dimensions: spatial distribution coupling and quantitative concentration
505 correlation. First, chlorophyll-a concentration spatial distribution (July-September 2021) was
506 retrieved from MODIS satellite data (see Fig. S18). The results show that high chlorophyll-a
507 concentrations are concentrated in coastal regions, with particularly prominent signals in the Bering

508 Strait and its vicinity. This reflects significant phytoplankton biomass accumulation in the area
509 during late summer and early autumn (Grebmeier et al., 2006), providing a potential site for biogenic
510 iodine enrichment.

511 To further verify the spatial association between high IO air masses and phytoplankton
512 enriched regions, backward trajectories of air masses during high IO concentration periods (Xuelong
513 2 cruise) were overlaid on MODIS chlorophyll-a concentration data (August 2021; see Fig. S19).
514 The results indicate that trajectories of high-probability IO sources extensively cover chlorophyll-a
515 hotspots, including the Bering Strait, southern Greenland, and coastal North Atlantic waters. This
516 directly confirms the spatial coupling between phytoplankton biological processes and IO formation
517 in these regions. Building on this spatial correlation and previous research, phytoplankton enrich
518 iodine in seawater via biological processes (e.g., cellular metabolism, death and decomposition) and
519 release iodine species across the sea-water-atmosphere interface (or sea ice brine channels). These
520 iodine species then participate in the photochemical production of IO (Saiz-Lopez et al., 2015).

521 To quantify the relationship between ship-based MAX-DOAS measured IO VCDs and
522 chlorophyll-a concentrations, MODIS chlorophyll-a data were averaged over a $0.1^\circ \times 0.1^\circ$ grid
523 within the daily coverage of ship-based IO observations. Correlation analysis with daily average IO
524 VCDs yielded a moderate positive correlation ($R=0.64$; Fig. 11), confirming biogenic sources as an
525 important contributor to IO. Factors contributing to the relatively weak correlation may include:
526 Satellite observational constraints: MODIS cannot detect phytoplankton communities within and
527 beneath sea ice, where the under-ice light environment and nutrient availability still support
528 phytoplankton growth. This leads to incomplete characterization of biogenic iodine potential by
529 chlorophyll-a retrievals (Saiz-Lopez et al., 2015); Confounding abiotic processes: IO concentrations
530 are also influenced by sea ice melting (which releases inorganic iodine) and photochemical
531 oxidation (which regulates iodine species transformation), weakening the correlation with
532 chlorophyll-a (Saiz-Lopez et al., 2015).

533



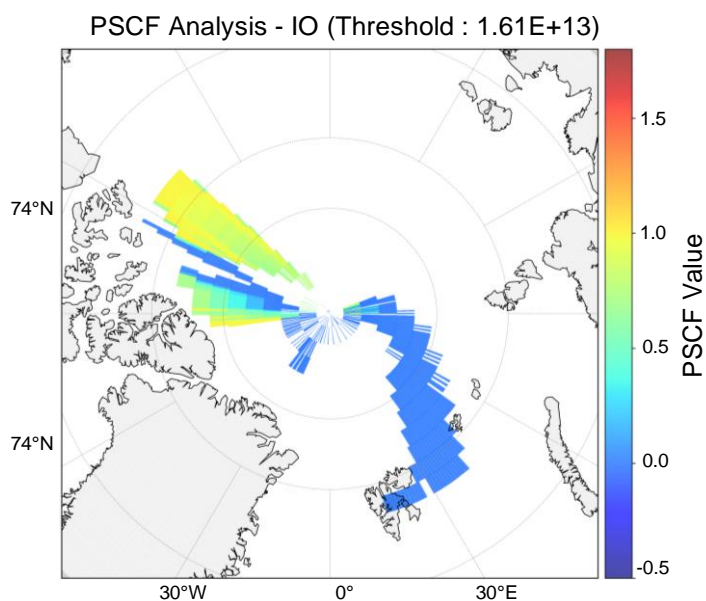
534

Fig. 11. Correlation between ship-based IO VCDs and Chlorophyll-a

535

Using backward trajectory data, PSCF analysis was performed to identify IO's potential source

536 regions and quantify their contributions to IO concentrations at the observation site (Fig. 12). To
537 delineate these source regions, ship-based high IO concentrations (threshold: 1.61×10^{13} molec./cm²)
538 were used as the benchmark. High probability potential IO sources are similar to those of BrO,
539 concentrated in western Greenland, the seas north of North America, and the Arctic sea-ice edge
540 zone. These regions likely support high phytoplankton biomass: phytoplankton enrich iodine in
541 seawater via metabolic processes and release iodine species to the atmosphere through sea-water-
542 atmosphere interface exchange. These species then participate in the photochemical production of
543 reactive iodine compounds (Mahajan et al., 2021).



544
545 **Fig. 12.** PSCF analysis for IO in the Arctic

546 Comparison of BrO and IO PSCF results reveals spatial differences in their potential source
547 regions: BrO sources are concentrated in high latitude sea-ice-covered areas, while IO sources are
548 centered in mid-to-low latitude coastal biologically active zones. In addition, correlation analysis of
549 ship-based BrO and IO VCDs (see Fig. S20) yielded a correlation coefficient $R=0.5$, indicating a
550 moderate association between the two. This result is reasonably explained by the PSCF identified
551 source region characteristics: Arctic BrO and IO derive from a shared ice-sea-atmosphere exchange
552 environment (e.g., material exchange interfaces in the sea ice edge zone), which provides a basis
553 for their correlation (Giesse et al., 2021; McFiggans et al., 2000; Saiz-Lopez et al., 2015); The
554 distinct source biases revealed by PSCF, namely BrO's dominance of sea ice sources and IO's
555 reliance on biogenic sources, result in a relatively weak correlation.

556

557 **4. Conclusion**

558 This study presents the spatial distributions of trace gases (NO_2 , HCHO, BrO, and IO) captured
559 during the 12th Chinese Arctic Scientific Expedition (July - September 2021) along a transect from
560 Shanghai to the Arctic. Utilizing ship-based Multi-Axis Differential Optical Absorption
561 Spectroscopy (MAX-DOAS), we establish a robust ground-truth baseline to assess the performance

562 of TROPOMI, GEMS, and GOME-2 satellite products in polar regions. Statistical analyses yield
563 correlation coefficients between 0.61 and 0.79, validating the efficacy of satellite remote sensing
564 for monitoring atmospheric composition over the Arctic and adjacent oceans. Our findings
565 demonstrate that tropospheric BrO is primarily controlled by Sea Ice Contact (SIC) duration, which
566 accounts for 48.63% of the variance in a GAM. Potential BrO source regions are identified in
567 western Greenland, the high-latitude Canadian Arctic, and the Marginal Ice Zone (MIZ). The R
568 value between BrO and SIC improved from 0.73 to 0.77 after incorporating dynamic boundary layer
569 height (BLH) constraints. Furthermore, meteorological conditions significantly modulate bromine
570 activation: southwesterly winds enhanced the correlation to 0.84, whereas snowfall weakened it
571 from 0.87 to 0.61. In contrast to the complex physico-chemical regulation of BrO, IO variability is
572 predominantly driven by biogenic emissions, correlating strongly with chlorophyll-a ($R=0.64$),
573 particularly in phytoplankton-rich regions like the Bering Strait. Notably, we observe a distinct
574 spatial divergence between the source regions of sea-ice-driven BrO and biogenic IO. However, a
575 moderate correlation ($R=0.5$) persists within the MIZ, suggesting that the ice-ocean-atmosphere
576 interface facilitates shared precursors or formation pathways for these reactive halogens. In
577 conclusion, this study provides high-precision validation for Arctic satellite retrievals and
578 systematically characterizes the drivers of polar halogen species. These data offer critical constraints
579 for optimizing emission parameterizations and halogen budget accounting in chemical transport
580 models, such as GEOS-Chem and WRF-Chem.

581
582 **Data availability.** All measurement data used in this study are publicly available at Zenodo via
583 the permanent DOI: <https://doi.org/10.5281/zenodo.18072720>. Additionally, they can also be made
584 available for scientific purposes upon request to the authors (Cheng Liu, chliu81@ustc.edu.cn, and
585 Chengzhi Xing, xingcz@aiofm.ac.cn).

586
587 **Author contributions.** QZ, CX and CL (Cheng Liu) designed the research and organized the
588 paper. QZ wrote the paper, while CX and CL (Cheng Liu) edited it. QZ, CX, YL, HP, WT, HL, CL
589 (Chao Liu), ZZ, WM and TT contributed to the retrieval of DOAS data and satellite data. QZ, CX,
590 YL, HP, WT, HL, CL (Chao Liu), ZZ, WM and TT contributed to data analysis. All the above-
591 mentioned authors contributed to the revision of the paper.

592
593 **Competing interests.** The contact author has declared that none of the authors has any
594 competing interests.

595
596 **Acknowledgements.** We would like to thank Zhouqing Xie's group for effectively organizing
597 the observation. We thank the National Oceanic and Atmospheric Administration (NOAA) Air
598 Resources Laboratory (ARL) for providing the open HYSPLIT transport and dispersion model.

599
600 **Financial support.** This study was supported by the National Natural Science Foundation of
601 China (grant nos. 42225504 and U21A2027), the President's Foundation of Hefei Institutes of
602 Physical Science, Chinese Academy of Sciences (grant no. BJPY2024B09, YZJJQY202401).

604 **Reference**

605 Adachi, K., Tobo, Y., Koike, M., Freitas, G., Zieger, P., and Krejci, R.: Composition and mixing
606 state of Arctic aerosol and cloud residual particles from long-term single-particle observations at
607 Zeppelin Observatory, Svalbard, *Atmospheric Chemistry and Physics*, 22, 14421-14439,
608 <https://doi.org/10.5194/acp-22-14421-2022>, 2022.

609 Begoin, M., Richter, A., Weber, M., Kaleschke, L., Tian-Kunze, X., Stohl, A., Theys, N., and
610 Burrows, J. P.: Satellite observations of long-range transport of a large BrO plume in the Arctic,
611 *Atmospheric Chemistry and Physics*, 10, 6515-6526, <https://doi.org/10.5194/acp-10-6515-2010>,
612 2010.

613 Behrens, L. K., Hilboll, A., Richter, A., Peters, E., Alvarado, L. M. A., Kalisz Hedegaard, A. B.,
614 Wittrock, F., Burrows, J. P., and Vrekoussis, M.: Detection of outflow of formaldehyde and glyoxal
615 from the African continent to the Atlantic Ocean with a MAX-DOAS instrument, *Atmospheric*
616 *Chemistry and Physics*, 19, 10257-10278, <https://doi.org/10.5194/acp-19-10257-2019>, 2019.

617 Blechschmidt, A.-M., Richter, A., Burrows, J. P., Kaleschke, L., Strong, K., Theys, N., Weber, M.,
618 Zhao, X., and Zien, A.: An exemplary case of a bromine explosion event linked to cyclone
619 development in the Arctic, *Atmospheric Chemistry and Physics*, 16, 1773-1788,
620 <https://doi.org/10.5194/acp-16-1773-2016>, 2016.

621 Bloss, W. J., Lee, J. D., Johnson, G. P., Sommariva, R., Heard, D. E., Saiz-Lopez, A., Plane, J. M.
622 C., McFiggans, G., Coe, H., Flynn, M., Williams, P., Rickard, A. R., and Fleming, Z. L.: Impact of
623 halogen monoxide chemistry upon boundary layer OH and HO₂ concentrations at a coastal site,
624 *Geophysical Research Letters*, 32, <https://doi.org/10.1029/2004GL022084>, 2005.

625 Bognar, K., Zhao, X., Strong, K., Chang, R. Y. W., Frieß, U., Hayes, P. L., McClure-Begley, A.,
626 Morris, S., Tremblay, S., and Vicente-Luis, A.: Measurements of Tropospheric Bromine Monoxide
627 Over Four Halogen Activation Seasons in the Canadian High Arctic, *Journal of Geophysical*
628 *Research: Atmospheres*, 125, e2020JD033015, <https://doi.org/10.1029/2020JD033015>, 2020.

629 Bougoudis, I., Blechschmidt, A.-M., Richter, A., Seo, S., Burrows, J. P., Theys, N., and Rinke, A.:
630 Long-term time series of Arctic tropospheric BrO derived from UV-VIS satellite remote sensing and
631 its relation to first-year sea ice, *Atmospheric Chemistry and Physics*, 20, 11869-11892,
632 <https://doi.org/10.5194/acp-20-11869-2020>, 2020.

633 Brockway, N., Peterson, P. K., Bigge, K., Hajny, K. D., Shepson, P. B., Pratt, K. A., Fuentes, J. D.,
634 Starn, T., Kaeser, R., Stirm, B. H., and Simpson, W. R.: Tropospheric bromine monoxide vertical
635 profiles retrieved across the Alaskan Arctic in springtime, *Atmospheric Chemistry and Physics*, 24,
636 23-40, <https://doi.org/10.5194/acp-24-23-2024>, 2024.

637 Cao, Y., Wang, Z., Liu, J., Ma, Q., Li, S., Liu, J., Li, H., Zhang, P., Chen, T., Wang, Y., Chu, B.,
638 Zhang, X., Saiz-Lopez, A., Francisco, J. S., and He, H.: Spontaneous Molecular Bromine Production
639 in Sea-Salt Aerosols, *Angewandte Chemie International Edition*,
640 <https://doi.org/10.1002/anie.202409779>, 2024.

641 Carlos Gómez Martín, J., Spietz, P., and Burrows, J. P.: Spectroscopic studies of the I₂/O₃
642 photochemistry, *Journal of Photochemistry and Photobiology A: Chemistry*, 176, 15-38,
643 <https://doi.org/10.1016/j.jphotochem.2005.09.024>, 2005.

644 Chan, K. L., Hartl, A., Lam, Y. F., Xie, P. H., Liu, W. Q., Cheung, H. M., Lampel, J., Poehler, D.,
645 Li, A., and Xu, J.: Observations of tropospheric NO₂ using ground-based MAX-DOAS and OMI
646 measurements during the Shanghai World Expo 2010, *Atmospheric Environment*, 119, 45-58,
647 <https://doi.org/10.1016/j.atmosenv.2015.08.041>, 2015.

648 Chan, K. L., Wiegner, M., Wenig, M., and Pöhler, D.: Observations of tropospheric aerosols and
649 NO₂ in Hong Kong over 5 years using ground-based MAX-DOAS, *Science of the Total Environment*,
650 619-620, 1545-1556, <https://doi.org/10.1016/j.scitotenv.2017.10.153>, 2018.

651 Chance, K. V. and Spurr, R. J. D.: Ring effect studies: Rayleigh scattering, including molecular
652 parameters for rotational Raman scattering, and the Fraunhofer spectrum, *Applied Optics*, AO, 36,
653 5224-5230, <https://doi.org/10.1364/AO.36.005224>, 1997.

654 Chen, Y., Liu, S., Zhu, L., Seo, S., Richter, A., Li, X., Ding, A., Sun, W., Shu, L., Wang, X., Valks,
655 P., Hendrick, F., Koenig, T. K., Volkamer, R., Bai, B., Wang, D., Pu, D., Sun, S., Li, J., Zuo, X., Fu,
656 W., Li, Y., Zhang, P., Yang, X., and Fu, T. M.: Global Observations of Tropospheric Bromine
657 Monoxide (BrO) Columns From TROPOMI, *Journal of Geophysical Research: Atmospheres*, 128,
658 e2023JD039091, <https://doi.org/10.1029/2023JD039091>, 2023.

659 Choi, S., Theys, N., Salawitch, R. J., Wales, P. A., Joiner, J., Canty, T. P., Chance, K., Suleiman, R.
660 M., Palm, S. P., Cullather, R. I., Darmenov, A. S., da Silva, A., Kurosu, T. P., Hendrick, F., and Van
661 Roozendael, M.: Link Between Arctic Tropospheric BrO Explosion Observed From Space and Sea-
662 Salt Aerosols From Blowing Snow Investigated Using Ozone Monitoring Instrument BrO Data and
663 GEOS-5 Data Assimilation System, *Journal of Geophysical Research: Atmospheres*, 123, 6954-
664 6983, <https://doi.org/10.1029/2017JD026889>, 2018.

665 Čížková, K., Lásková, K., Metelka, L., and Staněk, M.: Assessment of spectral UV radiation at
666 Marambio Base, Antarctic Peninsula, *Atmospheric Chemistry and Physics*, 23, 4617-4636,
667 <https://doi.org/10.5194/acp-23-4617-2023>, 2023.

668 Coburn, S., Dix, B., Sinreich, R., and Volkamer, R.: The CU ground MAX-DOAS instrument:
669 characterization of RMS noise limitations and first measurements near Pensacola, FL of BrO, IO,
670 and CHOCHO, *Atmospheric Measurement Techniques*, 4, 2421-2439, <https://doi.org/10.5194/amt-4-2421-2011>, 2011.

672 Crutzen, P. J.: The influence of nitrogen oxides on the atmospheric ozone content, *Quarterly Journal*
673 *of the Royal Meteorological Society*, 96, 320-325, <https://doi.org/10.1002/qj.49709640815>, 1970.

674 Cuevas, C. A., Maffezzoli, N., Corella, J. P., Spolaor, A., Vallelonga, P., Kjær, H. A., Simonsen, M.,
675 Winstrup, M., Vinther, B., Horvat, C., Fernandez, R. P., Kinnison, D., Lamarque, J. F., Barbante, C.,
676 and Saiz-Lopez, A.: Rapid increase in atmospheric iodine levels in the North Atlantic since the mid-
677 20th century, *Nature Communications*, 9, 1452, <https://doi.org/10.1038/s41467-018-03756-1>, 2018.

678 Dameris, M., Loyola, D. G., Nützel, M., Coldewey-Egbers, M., Lerot, C., Romahn, F., and van
679 Roozendaal, M.: Record low ozone values over the Arctic in boreal spring 2020, *Atmospheric*
680 *Chemistry and Physics*, 21, 617-633, <https://doi.org/10.5194/acp-21-617-2021>, 2021.

681 De Laat, A., Van Geffen, J., Stammes, P., Van Der A, R., Eskes, H., and Veefkind, J. P.: The Antarctic
682 stratospheric nitrogen hole: Southern Hemisphere and Antarctic springtime total nitrogen dioxide
683 and total ozone variability as observed by Sentinel-5p TROPOMI, *Atmospheric Chemistry and*
684 *Physics*, 24, 4511-4535, <https://doi.org/10.5194/acp-24-4511-2024>, 2024.

685 Fleischmann, O. C., Hartmann, M., Burrows, J. P., and Orphal, J.: New ultraviolet absorption cross-
686 sections of BrO at atmospheric temperatures measured by time-windowing Fourier transform
687 spectroscopy, *Journal of Photochemistry and Photobiology A: Chemistry*, 168, 117-132,
688 <https://doi.org/10.1016/j.jphotochem.2004.03.026>, 2004.

689 Frieß, U., Wagner, T., Pundt, I., Pfeilsticker, K., and Platt, U.: Spectroscopic measurements of
690 tropospheric iodine oxide at Neumayer Station, Antarctica, *Geophysical Research Letters*, 28, 1941-
691 1944, <https://doi.org/10.1029/2000GL012784>, 2001.

692 Frieß, U., Hollwedel, J., König-Langlo, G., Wagner, T., and Platt, U.: Dynamics and chemistry of
693 tropospheric bromine explosion events in the Antarctic coastal region, *Journal of Geophysical*
694 *Research (Atmospheres)*, 109, D06305, <https://doi.org/10.1029/2003JD004133>, 2004.

695 Frieß, U., Deutschmann, T., Gilfedder, B. S., Weller, R., and Platt, U.: Iodine monoxide in the
696 Antarctic snowpack, *Atmospheric Chemistry and Physics*, 10, 2439-2456,
697 <https://doi.org/10.5194/acp-10-2439-2010>, 2010.

698 Frieß, U., Sihler, H., Sander, R., Pöhler, D., Yilmaz, S., and Platt, U.: The vertical distribution of
699 BrO and aerosols in the Arctic: Measurements by active and passive differential optical absorption
700 spectroscopy, *Journal of Geophysical Research: Atmospheres*, 116,
701 <https://doi.org/10.1029/2011JD015938>, 2011.

702 Frieß, U., Klein Baltink, H., Beirle, S., Clémer, K., Hendrick, F., Henzing, B., Irie, H., de Leeuw,
703 G., Li, A., Moerman, M. M., van Roozendaal, M., Shaiganfar, R., Wagner, T., Wang, Y., Xie, P.,
704 Yilmaz, S., and Zieger, P.: Intercomparison of aerosol extinction profiles retrieved from MAX-
705 DOAS measurements, *Atmospheric Measurement Techniques*, 9, 3205-3222,
706 <https://doi.org/10.5194/amt-9-3205-2016>, 2016.

707 Frieß, U., Kreher, K., Querel, R., Schmithüsen, H., Smale, D., Weller, R., and Platt, U.: Source
708 mechanisms and transport patterns of tropospheric bromine monoxide: findings from long-term
709 multi-axis differential optical absorption spectroscopy measurements at two Antarctic stations,
710 *Atmospheric Chemistry and Physics*, 23, 3207-3232, <https://doi.org/10.5194/acp-23-3207-2023>,
711 2023.

712 Giesse, C., Notz, D., and Baehr, J.: On the Origin of Discrepancies Between Observed and
713 Simulated Memory of Arctic Sea Ice, *Geophysical Research Letters*, 48, e91784,
714 <https://doi.org/10.1029/2020GL091784>, 2021.

715 Gong, W., Beagley, S. R., Toyota, K., Skov, H., Christensen, J. H., Lupu, A., Pendlebury, D., Zhang,
716 J., Im, U., Kanaya, Y., Saiz-Lopez, A., Sommariva, R., Effertz, P., Halfacre, J. W., Jepsen, N., Kivi,
717 R., Koenig, T. K., Müller, K., Nordstrøm, C., Petropavlovskikh, I., Shepson, P. B., Simpson, W. R.,
718 Solberg, S., Staebler, R. M., Tarasick, D. W., Van Malderen, R., and Vestenius, M.: Modelling Arctic
719 lower-tropospheric ozone: processes controlling seasonal variations, *Atmospheric Chemistry and*
720 *Physics*, 25, 8355-8405, <https://doi.org/10.5194/acp-25-8355-2025>, 2025.

721 Grebmeier, J. M., Overland, J. E., Moore, S. E., Farley, E. V., Carmack, E. C., Cooper, L. W., Frey,
722 K. E., Helle, J. H., McLaughlin, F. A., and McNutt, S. L.: A Major Ecosystem Shift in the Northern
723 Bering Sea, *Science*, 311, 1461-1464, 2006.

724 Hao, Y., Li, P., Gou, Y., Wang, Z., Tian, M., Chen, Y., Kuang, Y., Xu, H., Wan, F., Luo, Y., Huang,
725 W., and Chen, J.: Divergent changes in aerosol optical hygroscopicity and new particle formation
726 during a heatwave of summer 2022, *Atmospheric Chemistry and Physics*, 25, 12811-12830,
727 <https://doi.org/10.5194/acp-25-12811-2025>, 2025.

728 Hara, K., Osada, K., Yabuki, M., Matoba, S., Hirabayashi, M., Fujita, S., Nakazawa, F., and
729 Yamanouchi, T.: Atmospheric sea-salt and halogen cycles in the Antarctic, *Environmental Science:*
730 *Processes and Impacts*, 22, 2003-2022, <https://doi.org/10.1039/D0EM00092B>, 2020.

731 Hendrick, F., Van Roozendaal, M., Chipperfield, M. P., Dorf, M., Goutail, F., Yang, X., Fayt, C.,
732 Hermans, C., Pfeilsticker, K., Pommereau, J.-P., Pyle, J. A., Theys, N., and De Mazière, M.:
733 Retrieval of stratospheric and tropospheric BrO profiles and columns using ground-based zenith-
734 sky DOAS observations at Harestua, 60° N, *Atmospheric Chemistry and Physics*, 7, 4869-
735 4885, <https://doi.org/10.5194/acp-7-4869-2007>, 2007.

736 Hindley, N. P., Wright, C. J., Smith, N. D., Hoffmann, L., Holt, L. A., Alexander, M. J., Moffat-
737 Griffin, T., and Mitchell, N. J.: Gravity waves in the winter stratosphere over the Southern Ocean:
738 high-resolution satellite observations and 3-D spectral analysis, *Atmospheric Chemistry and Physics*,
739 19, 15377-15414, <https://doi.org/10.5194/acp-19-15377-2019>, 2019.

740 Hong, Q., Liu, C., Chan, K. L., Hu, Q., Xie, Z., Liu, H., Si, F., and Liu, J.: Ship-based MAX-DOAS
741 measurements of tropospheric NO₂, SO₂, and HCHO distribution along the Yangtze River,
742 *Atmospheric Chemistry and Physics*, 18, 5931–5951, <https://doi.org/10.5194/acp-18-5931-2018>,
743 2018.

744 Hwang, J. H. and Kang, D. W.: Emission Control Routes in Liner Shipping between Korea and
745 Japan, *Journal of Marine Science and Engineering*, 11, 2250, <https://doi.org/10.3390/jmse11122250>,
746 2023.

747 Jozef, G. C., Cassano, J. J., Dahlke, S., Dice, M., Cox, C. J., and de Boer, G.: An overview of the
748 vertical structure of the atmospheric boundary layer in the central Arctic during MOSAiC,
749 *Atmospheric Chemistry and Physics*, 24, 1429–1450, <https://doi.org/10.5194/acp-24-1429-2024>,
750 2024.

751 Khosravi, S., Rinke, A., Dorn, W., Lüpkes, C., Gryanik, V., Chechin, D., Jaiser, R., and Handorf, D.:

752 The role of air-sea ice-ocean interaction processes for Arctic-midlatitude linkages,
753 <https://doi.org/10.5194/egusphere-egu2020-15116>, 2020.

754 Kuhlmann, G., Hartl, A., Cheung, H. M., Lam, Y. F., and Wenig, M. O.: A novel gridding algorithm
755 to create regional trace gas maps from satellite observations, *Atmospheric Measurement Techniques*,
756 7, 451–467, <https://doi.org/10.5194/amt-7-451-2014>, 2014.

757 Luo, Y., Si, F., Zhou, H., Dou, K., Liu, Y., and Liu, W.: Observations and source investigations of
758 the boundary layer bromine monoxide (BrO) in the Ny-Ålesund Arctic, *Atmospheric Chemistry and
759 Physics*, 18, 9789–9801, <https://doi.org/10.5194/acp-18-9789-2018>, 2018.

760 Mahajan, A. S., Biswas, M. S., Beirle, S., Wagner, T., Schönhardt, A., Benavent, N., and Saiz-Lopez,
761 A.: Observations of iodine monoxide over three summers at the Indian Antarctic bases of Bharati
762 and Maitri, *Atmospheric Chemistry and Physics*, 21, 11829–11842, <https://doi.org/10.5194/acp-21-11829-2021>, 2021.

764 Mahajan, A. S., Wagh, S., Fernandez, R. P., Singh, S., Bucci, S., and Saiz-Lopez, A.: Differences in
765 iodine chemistry over the Antarctic continent, *Polar Science*, 40, 101014,
766 <https://doi.org/10.1016/j.polar.2023.101014>, 2024.

767 McFiggans, G., Plane, J. M. C., Allan, B. J., Carpenter, L. J., Coe, H., and O’Dowd, C.: A modeling
768 study of iodine chemistry in the marine boundary layer, *Journal of Geophysical Research
769 Atmospheres*, 105, 14371–14385, <https://doi.org/10.1029/1999JD901187>, 2000.

770 McPhee, M. G.: The sea ice–ocean boundary layer, Book Title: *Sea Ice*. DOI:
771 10.1002/9781118778371.ch5, 138–159, <https://doi.org/10.1002/9781118778371.ch5>, 2017.

772 Meller, R. and Moortgat, G. K.: Temperature dependence of the absorption cross sections of
773 formaldehyde between 223 and 323 K in the wavelength range 225–375 nm, *Journal of Geophysical
774 Research Atmospheres*, 105, 7089–7101, <https://doi.org/10.1029/1999JD901074>, 2000.

775 Moore, C. W., Obrist, D., Steffen, A., Staebler, R. M., Douglas, T. A., Richter, A., and Nghiem, S.
776 V.: Convective forcing of mercury and ozone in the Arctic boundary layer induced by leads in sea
777 ice, *Nature*, 506, 81–84, <https://doi.org/10.1038/nature12924>, 2014.

778 Nasse, J.-M., Zielcke, J., Frieß, U., Lampel, J., König-Langlo, G., and Platt, U.: Inference of cloud
779 altitude and optical properties from MAX-DOAS measurements, *EGU General Assembly
780 Conference Abstracts*, ADS Bibcode: 2015 EGUGA.17.7232N, 7232, 2015a.

781 Nasse, J.-M., Zielcke, J., Lampel, J., Buxmann, J., Frieß, U., and Platt, U.: Vertical distribution of
782 tropospheric BrO in the marginal sea ice zone of the Northern Weddell Sea, *EGU General Assembly
783 Conference Abstracts*, ADS Bibcode: 2015 EGUGA.17.7150N, 7150, 2015b.

784 Park, J., Kang, H., Gim, Y., Jang, E., Park, K.-T., Park, S., Jung, C. H., Ceburnis, D., O’Dowd, C.,
785 and Yoon, Y. J.: New particle formation leads to enhanced cloud condensation nuclei concentrations
786 on the Antarctic Peninsula, *Atmospheric Chemistry and Physics*, 23, 13625–13646,
787 <https://doi.org/10.5194/acp-23-13625-2023>, 2023.

788 Pernov, J. B., Bossi, R., Lebourgeois, T., Nøjgaard, J. K., Holzinger, R., Hjorth, J. L., and Skov, H.:

789 Atmospheric VOC measurements at a High Arctic site: characteristics and source apportionment,
790 Atmospheric Chemistry and Physics, 21, 2895–2916, <https://doi.org/10.5194/acp-21-2895-2021>,
791 2021.

792 Peterson, P. K., Pöhler, D., Sihler, H., Zielcke, J., General, S., Frieß, U., Platt, U., Simpson, W. R.,
793 Nghiem, S. V., Shepson, P. B., Stirm, B. H., Dhaniyala, S., Wagner, T., Caulton, D. R., Fuentes, J.
794 D., and Pratt, K. A.: Observations of bromine monoxide transport in the Arctic sustained on aerosol
795 particles, Atmospheric Chemistry and Physics, 17, 7567–7579, [https://doi.org/10.5194/acp-17-](https://doi.org/10.5194/acp-17-7567-2017)
796 7567-2017, 2017.

797 Polissar, A. V., Hopke, P. K., and Harris, J. M.: Source regions for atmospheric aerosol measured at
798 Barrow, Alaska, Environmental Science and Technology, 35, 4214–4226,
799 <https://doi.org/10.1021/es0107529>, 2001.

800 Polvani, L. M., Previdi, M., England, M. R., Chiodo, G., and Smith, K. L.: Substantial twentieth-
801 century Arctic warming caused by ozone-depleting substances, Nature Climate Change., 10, 130–
802 133, <https://doi.org/10.1038/s41558-019-0677-4>, 2020.

803 Prados-Roman, C., Gómez-Martín, L., Puente-dura, O., Navarro-Comas, M., Iglesias, J., de Mingo,
804 J. R., Pérez, M., Ochoa, H., Barlasina, M. E., Carbajal, G., and Yela, M.: Reactive bromine in the
805 low troposphere of Antarctica: estimations at two research sites, Atmospheric Chemistry and
806 Physics, 18, 8549–8570, <https://doi.org/10.5194/acp-18-8549-2018>, 2018.

807 Pratt, K. A., Custard, K. D., Shepson, P. B., Douglas, T. A., Pöhler, D., General, S., Zielcke, J.,
808 Simpson, W. R., Platt, U., Tanner, D. J., Gregory Huey, L., Carlsen, M., and Stirm, B. H.:
809 Photochemical production of molecular bromine in Arctic surface snowpacks, Nature Geosci, 6,
810 351–356, <https://doi.org/10.1038/ngeo1779>, 2013.

811 Ranjithkumar, A., Duncan, E., Yang, X., Partridge, D., and Frey, M.: Modelling sea-salt aerosol flux
812 from blowing snow over a changing sea ice environment, EGU General Assembly Conference
813 Abstracts, EGU-6988, <https://doi.org/10.5194/egusphere-egu23-6988>, 2023.

814 Richter, A., Wittrock, F., Eisinger, M., and Burrows, J. P.: GOME observations of tropospheric BrO
815 in northern hemispheric spring and summer 1997, Geophysical Research Letters, 25, 2683–2686,
816 <https://doi.org/10.1029/98GL52016>, 1998.

817 Roy, R., Kumar, P., Kuttippurath, J., and Lefevre, F.: Chemical ozone loss and chlorine activation
818 in the Antarctic winters of 2013–2020, Atmospheric Chemistry and Physics, 24, 2377–2386,
819 <https://doi.org/10.5194/acp-24-2377-2024>, 2024.

820 Rozanov, A., Rozanov, V., Buchwitz, M., Kokhanovsky, A., and Burrows, J. P.: SCIATRAN 2.0 –
821 A new radiative transfer model for geophysical applications in the 175–2400 nm spectral region,
822 Advances in Space Research, 36, 1015–1019, <https://doi.org/10.1016/j.asr.2005.03.012>, 2005.

823 Saiz-Lopez, A., Mahajan, A. S., Salmon, R. A., Bauguitte, S. J.-B., Jones, A. E., Roscoe, H. K., and
824 Plane, J. M. C.: Boundary Layer Halogens in Coastal Antarctica, Science, 317, 348–351,
825 <https://doi.org/10.1126/science.1141408>, 2007.

826 Saiz-Lopez, A., Plane, J. M. C., Mahajan, A. S., Anderson, P. S., Bauguitte, S. J.-B., Jones, A. E.,
827 Roscoe, H. K., Salmon, R. A., Bloss, W. J., Lee, J. D., and Heard, D. E.: On the vertical distribution
828 of boundary layer halogens over coastal Antarctica: implications for O₃, HO_x, NO_x and the Hg
829 lifetime, *Atmospheric Chemistry and Physics*, 8, 887–900, <https://doi.org/10.5194/acp-8-887-2008>,
830 2008.

831 Saiz-Lopez, A., Baidar, S., Cuevas, C. A., Koenig, T. K., Fernandez, R. P., Dix, B., Kinnison, D. E.,
832 Lamarque, J.-F., Rodriguez-Lloveras, X., Campos, T. L., and Volkamer, R.: Injection of iodine to
833 the stratosphere, *Geophysical Research Letters*, 42, 6852–6859,
834 <https://doi.org/10.1002/2015GL064796>, 2015.

835 Seo, S., Richter, A., Blechschmidt, A.-M., Bougoudis, I., and Burrows, J. P.: Spatial distribution of
836 enhanced BrO and its relation to meteorological parameters in Arctic and Antarctic sea-ice regions,
837 *Atmospheric Chemistry and Physics*, 20, 12285–12312, <https://doi.org/10.5194/acp-20-12285-2020>,
838 2020.

839 Serdyuchenko, A., Gorshelev, V., Weber, M., Chehade, W., and Burrows, J. P.: High spectral
840 resolution ozone absorption cross-sections and ndash; Part 2: Temperature dependence,
841 *Atmospheric Measurement Techniques*, 7, 625–636, <https://doi.org/10.5194/amt-7-625-2014>, 2014.

842 Shupe, M. D., Persson, P. O. G., Brooks, I. M., Tjernström, M., Sedlar, J., Mauritsen, T., Sjogren,
843 S., and Leck, C.: Cloud and boundary layer interactions over the Arctic sea-ice in late summer,
844 *Atmospheric Chemistry and Physics*, 13, 9379–9399, <https://doi.org/10.5194/acp-13-9379-2013>,
845 2013.

846 Simpson, W. R., Peterson, P. K., Frieß, U., Sihler, H., Lampel, J., Platt, U., Moore, C., Pratt, K.,
847 Shepson, P., Halfacre, J., and Nghiem, S. V.: Horizontal and vertical structure of reactive bromine
848 events probed by bromine monoxide MAX-DOAS, *Atmospheric Chemistry and Physics*, 17, 9291–
849 9309, <https://doi.org/10.5194/acp-17-9291-2017>, 2017.

850 Song, Y., Xing, C., Liu, C., Lin, J., Wu, H., Liu, T., Lin, H., Zhang, C., Tan, W., Ji, X., Liu, H., and
851 Li, Q.: Evaluation of transport processes over North China Plain and Yangtze River Delta using
852 MAX-DOAS observations, *Atmospheric Chemistry and Physics*, 23, 1803–1824,
853 <https://doi.org/10.5194/acp-23-1803-2023>, 2023.

854 Spagnesi, A., Barbaro, E., Feltracco, M., Scoto, F., Vecchiato, M., Vardè, M., Mazzola, M., Burgay,
855 F. Y., Bruschi, F., Hoppe, C. J. M., Bailey, A., Gambaro, A., Barbante, C., and Spolaor, A.: Impact
856 of Arctic Amplification variability on the chemical composition of the snowpack in Svalbard, *EGU*
857 *sphere*, 1–25, <https://doi.org/10.5194/egusphere-2024-1393>, 2024.

858 Stutz, J. and Platt, U.: Numerical analysis and estimation of the statistical error of differential optical
859 absorption spectroscopy measurements with least-squares methods, *Applied Optics*, AO, 35, 6041–
860 6053, <https://doi.org/10.1364/AO.35.006041>, 1996.

861 Stutz, J., Kim, E. S., Platt, U., Bruno, P., Perrino, C., and Febo, A.: UV-visible absorption cross
862 sections of nitrous acid, *Journal of Geophysical Research*, 105, 14,585–14,592,

863 <https://doi.org/10.1029/2000JD900003>, 2000.

864 Swanson, W. F., Graham, K. A., Halfacre, J. W., Holmes, C. D., Shepson, P. B., and Simpson, W.
865 R.: Arctic Reactive Bromine Events Occur in Two Distinct Sets of Environmental Conditions: A
866 Statistical Analysis of 6 Years of Observations, *Journal of Geophysical Research: Atmospheres*, 125,
867 e2019JD032139, <https://doi.org/10.1029/2019JD032139>, 2020.

868 Tack, F., Hendrick, F., Goutail, F., Fayt, C., Merlaud, A., Pinaridi, G., Hermans, C., Pommereau, J.-
869 P., and Van Roozendael, M.: Tropospheric nitrogen dioxide column retrieval from ground-based
870 zenith–sky DOAS observations, *Atmospheric Measurement Techniques*, 8, 2417–2435,
871 <https://doi.org/10.5194/amt-8-2417-2015>, 2015.

872 Tan, W., Liu, C., Wang, S., Xing, C., Su, W., Zhang, C., Xia, C., Liu, H., Cai, Z., and Liu, J.:
873 Tropospheric NO₂, SO₂, and HCHO over the East China Sea, using ship-based MAX-DOAS
874 observations and comparison with OMI and OMPS satellite data, *Atmospheric Chemistry and
875 Physics*, 18, 15387–15402, <https://doi.org/10.5194/acp-18-15387-2018>, 2018.

876 Thalman, R. and Volkamer, R.: Temperature dependent absorption cross-sections of O₂-O₂ collision
877 pairs between 340 and 630 nm and at atmospherically relevant pressure, *Physical Chemistry
878 Chemical Physics*, 15, 15371–15381, <https://doi.org/10.1039/c3cp50968k>, 2013.

879 Theys, N., Van Roozendael, M., Hendrick, F., Yang, X., De Smedt, I., Richter, A., Begoin, M., Errera,
880 Q., Johnston, P. V., Kreher, K., and De Mazière, M.: Global observations of tropospheric BrO
881 columns using GOME-2 satellite data, *Atmospheric Chemistry and Physics*, 11, 1791–1811,
882 <https://doi.org/10.5194/acp-11-1791-2011>, 2011.

883 Tremblay, S., Picard, J.-C., Bachelder, J. O., Lutsch, E., Strong, K., Fogal, P., Leaitch, W. R., Sharma,
884 S., Kolonjari, F., Cox, C. J., Chang, R. Y.-W., and Hayes, P. L.: Characterization of aerosol growth
885 events over Ellesmere Island during the summers of 2015 and 2016, *Atmospheric Chemistry and
886 Physics*, 19, 5589–5604, <https://doi.org/10.5194/acp-19-5589-2019>, 2019.

887 Vandaele, A. C., Hermans, C., Simon, P. C., Carleer, M., Colin, R., Fally, S., Mérienne, M. F.,
888 Jenouvrier, A., and Coquart, B.: Measurements of the NO₂ absorption cross-section from 42000
889 cm⁻¹ to 10 000 cm⁻¹ (238–1000 nm) at 220 K and 294 K, *Journal of Quantitative Spectroscopy and
890 Radiative Transfer*, 59, 171–184, [https://doi.org/10.1016/S0022-4073\(97\)00168-4](https://doi.org/10.1016/S0022-4073(97)00168-4), 1998.

891 Wagner, T., Ibrahim, O., Sinreich, R., Frieß, U., von Glasow, R., and Platt, U.: Enhanced
892 tropospheric BrO over Antarctic sea-ice in mid-winter observed by MAX-DOAS on board the
893 research vessel Polarstern, *Atmospheric Chemistry and Physics*, 7, 3129–3142,
894 <https://doi.org/10.5194/acp-7-3129-2007>, 2007.

895 Wagner, T., Ibrahim, O., Shaiganfar, R., and Platt, U.: Mobile MAX-DOAS observations of
896 tropospheric trace gases, *Atmospheric Measurement Techniques*, 3, 129–140,
897 <https://doi.org/10.5194/amt-3-129-2010>, 2010.

898 Wang, X., Shen, Y., Lin, Y., Pan, J., Zhang, Y., Louie, P. K. K., Li, M., and Fu, Q.: Ambient
899 measurement of shipping emissions in Shanghai port areas, <https://doi.org/10.5194/acp-2018-737>,

900 21 August 2018.

901 Welsh, B. A., Corrigan, M. E., Assaf, E., Nauta, K., Sebastianelli, P., Jordan, M. J. T., Fittschen, C.,
902 and Kable, S. H.: Photophysical oxidation of HCHO produces HO₂ radicals, *Nature Chemistry*, 15,
903 1350–1357, <https://doi.org/10.1038/s41557-023-01272-4>, 2023.

904 Wittrock, F., Oetjen, H., Richter, A., Fietkau, S., Medeke, T., Rozanov, A., and Burrows, J. P.: MAX-
905 DOAS measurements of atmospheric trace gases in Ny-Ålesund - Radiative transfer studies and
906 their application, *Atmospheric Chemistry and Physics*, 4, 955–966, [https://doi.org/10.5194/acp-4-](https://doi.org/10.5194/acp-4-955-2004)
907 955-2004, 2004.

908 Wu, F., Xie, P., Li, A., Mou, F., Chen, H., Zhu, Y., Zhu, T., Liu, J., and Liu, W.: Investigations of
909 temporal and spatial distribution of precursors SO₂ and NO₂ vertical columns in the North China
910 Plain using mobile DOAS, *Atmospheric Chemistry and Physics*, 18, 1535–1554,
911 <https://doi.org/10.5194/acp-18-1535-2018>, 2018.

912 Yang, X., Blechschmidt, A.-M., Bogner, K., McClure-Begley, A., Morris, S., Petropavlovskikh, I.,
913 Richter, A., Skov, H., Strong, K., Tarasick, D. W., Uttal, T., Vestenius, M., and Zhao, X.: Pan-Arctic
914 surface ozone: modelling vs. measurements, *Atmospheric Chemistry and Physics*, 20, 15937–15967,
915 <https://doi.org/10.5194/acp-20-15937-2020>, 2020.

916 Yang, Y., Zhao, C., Wang, Q., Cong, Z., Yang, X., and Fan, H.: Aerosol characteristics at the three
917 poles of the Earth as characterized by Cloud–Aerosol Lidar and Infrared Pathfinder Satellite
918 Observations, *Atmospheric Chemistry and Physics*, 21, 4849–4868, [https://doi.org/10.5194/acp-21-](https://doi.org/10.5194/acp-21-4849-2021)
919 4849-2021, 2021.

920 Yin, X., Kang, S., de Foy, B., Ma, Y., Tong, Y., Zhang, W., Wang, X., Zhang, G., and Zhang, Q.:
921 Multi-year monitoring of atmospheric total gaseous mercury at a remote high-altitude site (Nam Co,
922 4730m a.s.l.) in the inland Tibetan Plateau region, *Atmospheric Chemistry and Physics*, 18, 10557–
923 10574, <https://doi.org/10.5194/acp-18-10557-2018>, 2018.

924 Zhao, X., Strong, K., Adams, C., Schofield, R., Yang, X., Richter, A., Friess, U., Blechschmidt, A.-
925 M., and Koo, J.-H.: A case study of a transported bromine explosion event in the Canadian high
926 arctic, *Journal of Geophysical Research: Atmospheres*, 121, 457–477,
927 <https://doi.org/10.1002/2015JD023711>, 2016.

928